APPLICATION OF THE SLOPE PARAMETER APPROACH TO CATHODIC PROTECTION DESIGN OF CONDUCTOR ARRAYS ON OFFSHORE STRUCTURES

Patrick Pierson and William H. Hartt
Center for Marine Materials
Department of Ocean Engineering
Florida Atlantic University
777 Glades Road
Boca Raton, FL 33431

ABSTRACT

The difficulty of designing and providing adequate cathodic protection for conductor arrays on offshore structures has been recognized historically. Limitations of the presently practiced cathodic protection design procedure for this specific application are reviewed, and advantages and shortcomings of the recently proposed slope parameter approach are evaluated. A procedure for calculating the resistance of a conductor array is introduced, and it is demonstrated how the slope parameter can be determined from this, along with the optimum anode design, including size, shape and number. An experiment was performed where resistance of a miniaturized, simulated conductor array was measured in sea water; and the results are compared with those from the analytical design method.

Key Words: Cathodic protection, cathodic protection design, slope parameter, offshore structures, conductors, resistance equations.

INTRODUCTION

Present Cathodic Protection Design Practice

Cathodic protection, either alone or in conjunction with coatings, has evolved to the point where it has been for several decades the principle corrosion control methodology of choice for the submerged portion of offshore structures, including ships, pipelines, and petroleum production platforms. For the latter two structure types (pipelines and platforms) sacrificial anode cathodic protection is normally employed because of its practicality and greater reliability compared to impressed current. Present recommended practices, which address the design of marine sacrificial anode cathodic protection systems (1,2), are based upon determination of the current

output per sacrificial anode, I_a, as calculated from Ohm's law according to the expression

$$I_a = \frac{\phi_c - \phi_a}{R_a},$$

(1

where

ϕ_c = closed circuit cathode potential,
ϕ_a = closed circuit anode potential and
R_a = resistance of an individual anode, which for spaceframe structures is typically the dominant component of the total circuit resistance.

Anode resistance to remote earth is normally determined from theoretical numerical expressions which have been established in terms of anode dimensions and electrolyte resistivity (1-2). From the net current for protection, $i_c \cdot A_c$, the required number of anodes, N, is calculated from the relationship

$$N = \frac{i_c \cdot A_c}{I_a},$$

(2

where

i_c = cathode current density and
A_c = cathode surface area.

The present design approach (1,2) incorporates the principle of rapid polarization (3-6) whereby a relatively high initial current density, i_i, is applied such that a structure potential near -1.00 v (Ag/AgCl) is achieved "...within a reasonably short period of time" (2) as a consequence of formation of a particularly protective calcareous deposit (7-13). This latter protocol involves specification of three design current densities: i_i, i_m (the mean or average current density), and i_f (final current density) with the required number of anodes corresponding to i_i and i_f being calculated according to Equations 1 and 2. Determination of N corresponding to i_m utilizes the expression

$$N = \frac{i_m \cdot A_c \cdot T}{C \cdot w},$$

(3

where

T = design life,
C = anode current capacity, and
w = weight of an individual anode.

The objective of this latter determination is to confirm that adequate anode mass to achieve the current output for the design life is available.

Z

Slope Parameter Approach to Cathodic Protection Design

Recently, a novel, first principles based sacrificial anode cathodic protection methodology was introduced (13,14). This is based upon a modified form of Ohm's Law according to the relationship

$$\phi_c = \left(R_t \cdot A_c\right)i_c + \phi_a,$$

(4

where $R_t = R_a + R_c + R_x$ with R_c and R_x being the cathode and sum of any external resistances, respectively. For space frame offshore structures with multiple, distributed anodes, $R_t \approx R_a/N$, and so Equation 4 becomes

$$\phi_a = \left(\frac{R_a \cdot A_c}{N}\right)i_c + \phi_a.$$

(5

Here, $R_t \cdot A_c$ is designated the slope parameter, S. Also, Equation 3 may be written in a modified form as

$$Nw = i_m \cdot T \cdot A_c \cdot K,$$

(6

where K is the anode consumption rate or the inverse of current capacity. From this, it follows that

$$R_a \cdot w = i_m \cdot T \cdot K \cdot S.$$

(7

This relationship implicitly reflects both the cp design per se and parameters relevant to anode size and number, and it serves as the basis for the proposed design approach. Thus, the protocol involves specification of each of the four terms on the right hand side of Equation 7 according to anode material properties and design choices. Particularly important in this regard is definition of the value for S. Once all terms on the right side are selected, the process is reduced to determination of the optimum combination of R_a and w. This may be accomplished in terms of anodes of standard dimensions or by a unique anode design (size, shape, and weight), as discussed below. The required number of anodes can then be calculated from Equation 3 or 6.

Various aspects of the slope parameter approach, in comparison to the presently practiced procedure, are apparent from Figure 1 which illustrates schematically both the dynamic polarization curve for steel upon initial sea water exposure and the long-term ϕ-i interrelationship which ultimately develops (14). The former reflects minimal oxygen concentration polarization, and any cathodic polarization process must begin at some point upon this curve. The long-term curve, on the other hand, exhibits a sigmoidal shape in association with formation of a particularly protective calcareous deposit in the potential range from -0.90 to -1.05 v (Ag/AgCl); and the final state for a particular cathodic polarization situation must lie upon this. Superimposed upon this plot are different design alternatives, as represented

by four slope parameter choices*. Thus, a design, according to slope S_1 results in inadequate protection, since the polarized potential does not achieve the minimum value for the arrestment of corrosion (-0.80 v (Ag/AgCl)). Alternately, slope S_2 probably provides protection but at a potential for which current density is relatively high. Slopes in the range S_3 to S_4, however, provide polarization to the potential range where i_m is minimum.

Of specific interest in this paper is the challenge presented to cathodic protection design by components upon offshore structures such as conductor arrays. This arises because the grouping of such components results in shielding of the back sides and inner members from the cp current. Present industry practice involves including the conductor surface area in determination of the net value for A_c and possibly concentrating anodes close to the conductors. However, this approach has not been entirely satisfactory, as evidenced by problems that have been reported (15); and the conductor area is generally recognized as a potential corrosion control problem. The present paper addresses this difficulty from the standpoint of, first, the additional electrical resistance associated with the geometry of a conductor array and, second, utility of the slope parameter approach to cathodic protection design for this specific member type.

Individual and Collective Electrode Resistance Equations

The resistance to ground of individual electrodes of various geometries has been addressed historically by numerous authors (16-20). The case of closely spaced electrodes, however, is more complex and less attended; and it is this situation that is relevant in the case of conductors on offshore structures. In this regard, consider the specific case of sixteen 0.51 m (20 inch) diameter conductors equally spaced 2.29 m apart in a square array in 300 m deep water, as shown schematically in Figure 2. The resistance to ground of this array (the R_c component of the R_t term in Equation 4) was evaluated using an approach based upon Sunde's submerged equation for the resistance of n parallel electrodes of identical length spaced equally about the circumference of a circle, $R(n)$ (21,22), as

$$R(n) = \frac{1}{n}\left[R1(r) + \sum_{m=1}^{n-1} R1(D\sin(m\pi/n))\right], \tag{8}$$

where D is the diameter of the circle (cm) and R1 and $R1(D\sin(m\pi/n))$ are generated by the average potential method from Sunde's equation for the resistance of a single, deeply submerged cylindrical electrode as

$$R1(r_i) = \left[\frac{\rho}{2\pi L}\right]\left[\ln\left[\frac{L\left(1 + \sqrt{1 + (r/L)^2}\right)}{r}\right] + \frac{r}{L} - \sqrt{1 + (r/L)^2}\right], \tag{9}$$

for which $r_i = \{r, D\sin(m\pi/n)\}$ and where

---

* Note that specification of a particular slope parameter is synonymous with choosing an initial current density at a particular potential.

4

ρ is electrolyte resistivity (Ohm.cm),
L is electrode length (cm), and
r is electrode radius (cm).

For four identical electrodes equally spaced about a circle, as shown in Figure 3, Equation 8 becomes (21)

$$R(n = 4) = \frac{1}{4}\left[R1(r) + 2\left[R1(D\sin(\pi/4))\right] + R1(D)\right].$$ (10

Resistance of the 16 electrode array (Figure 2) was evaluated by considering it as four sub-groups of four electrodes (Figure 3), calculating the resistance of each subgroup using Equation 10, replacing the four electrodes of a subgroup with a centrally positioned single electrode of equivalent resistance as determined from Dwight's equation for a fully submerged electrode,

$$R = \frac{\rho}{2\pi L}\left[\ln\left(\frac{2L}{r}\right) - 1\right],$$ (11

and reapplying Equation 10 to the quadrapole of four, equivalent resistance electrodes. This process is illustrated schematically in Figure 4.

It was determined that in 300 m deep water 140 329 kg aluminum anodes of standard dimensions are required to protect this conductor array according to the design procedure detailed in NACE RP0176-94 (1), assuming $i_i = 110$ mA/m^2 and $R_a = 0.041 \ \Omega$. Figure 5 plots resistance of such an anode array as a function of water depth. Thus, this resistance decreases with increasing depth because of the progressively greater number of anodes that is required. Of course, whether or not protection is achieved depends upon anode positioning such that current reaches 1) the inner conductors and 2) the backside of all conductors, since the design calculations do not take interference or shielding into account.

Figure 6 shows the resistance for the conductor array as a function of water depth, as determined from Equation 10 and the above described method. Both the conductor array and anode resistances, as well as the sum of the two, are shown in Figure 7. Thus, the conductor resistance becomes an increasing fraction of the total as water depth increases such that this resistance is about one-half that of the anode at 15 m and exceeds the anode resistance for depths beyond about 75 m.

Application of the Slope Parameter to Cathodic Protection Design of Conductor Arrays

The slope parameter provides an alternative approach to cathodic protection design, as noted above. Thus, Equation 7 can be used to calculate the necessary weight of individual anodes (w) and Equation 6 to determine N. This indicates that 140 225 kg anodes are adequate*, as compared to the same

---

* This calculation assumed that resistance of the reduced mass anode (225 kg instead of 329 kg) was unchanged at 0.041 Ω. The possibility that it may be impractical to use such an anode was not considered.

number of 329 kg anodes according to the conventional method. Such a material savings in conjunction with this new design method has been discussed previously (14). However, as was the case with the conventional design approach (see above), the slope parameter method, in and of itself, also does not consider interference effects.

Figure 8 plots steady-state ϕ-i data and the corresponding best-fit sigmoidal curve for a series of laboratory specimens, each of which was polarized in quiescent sea water according to a different slope parameter (14). Superimposed upon this curve is the slope parameter design line which considers 1) anode resistance only (S = 2.28 $\Omega \cdot m^2$) and 2) both anode and cathode resistances. The latter of these shows results for water depths of 30, 100, and 300 m. Thus, for the case where anode resistance only is considered,

$$S = \frac{R_a \cdot A_c}{N},$$
(12

and where both anode and cathode resistances are taken into account,

$$S = R_t \cdot A_c = \left(\frac{R_a}{N} + R_c\right)A_c.$$
(13

Figure 8 indicates that design according to RP0176 would be adequate if there were no interference or shielding between the consuctors, since the intersection of the design line with the steady-state ϕ-i curve occurs in the potential range of protection ($\phi \leq$ -0.80 v (Ag/AgCl)) and where current density is minimum. However, if conductor resistance is considered and the same number of anodes forecast by RP0176 are employed, then current density may be 2.5 times higher than the minimum value; and the structure is either underprotected (water depths 100 and 300 m) or marginally protected (water depth 30 m). An appropriate slope parameter (2.28 $\Omega \cdot m^2$, for example) can be achieved using Equation 13 by reducing R_a or increasing N (or both) or in terms of Equation 7 by setting $R_a \cdot w$ (left side of Equation 7) to the appropriate value and optimizing the components of this product (14).

It should be recognized that, while a cathodic protection design which incorporates conductor resistance facilitates definition of the appropriate anode design (size, shape, and weight) and number, it does not ensure that all areas of the array are protected. This follows because the slope parameter for an array is an averaged value, where S is lowest on the outer surfaces of the outer conductors and highest on the back face of the inner ones. There is a tendency for protection to ultimately spread to these shielded areas, however, as current demand upon the outer areas decreases due to calcareous deposit formation, provided that the net anode current output is adequate and IR drop to the inner areas is not excessive.

An additional consideration pertains to what is termed the "effective depth" of a conductor array for purposes of calculating the cathode resistance. Thus, in the case where the anodes provide a uniform current field, there

should exist drainage points upon the conductors at each horizontal framing level for which there are conductor guides (this assumes that the conductor guides provide a low resistance connection between the conductors and structure). If this is the case, then no net current to the conductors should cross the plane of the horizontal framing. On this basis, the conductor array depth for the purpose of determining resistance and slope parameter for this component should be the horizontal framing interval. Considering, for example, that this interval is 30 m, then the Equation 10 calculation is performed using this dimension for the conductor depth; and the number of anodes determined therefrom is multiplied by the number of such bays.

Experimental Verification

An experiment was performed where resistance of a down-scaled, simulated conductor array was measured in order to determine accuracy of the above design method. This utilized a 3.05 m wide by 4.57 m long by 0.91 m deep coated steel sea water test tank and the electrode arrangement shown in Figure 9. The central electrode consisted of 16 electrically interconnected 3.18 mm diameter by 0.584 m long steel rods in a square array with a 14.3 mm centerline rod spacing which were mounted at each end in a plastic holder. This resulted in the same rod radius-to-spacing ratio as for the conductor array that was evaluated above. The simulated conductor array was surrounded by four electrically interconnected 12.7 mm diameter by 0.584 m long steel rods, each of which was positioned 0.56 m from the conductor array centerline, which represented anodes. It was intended that this simulate electrically a situation where a conductor array is being cathodically protected by remotely positioned anodes.

Figure 10 shows the electrical circuit for the electrode arrangement in Figure 9, which is represented analytically by the equation

$$R_c = R_m - R_3 - \left(\frac{R_1 + R_a}{4}\right),\qquad(14$$

where

R_c is the conductor array resistance,
R_1 and R_3 are the lead wire resistances to the simulated anodes and conductor, respectively (0.100 and 0.025 Ω), and
R_m is the measured resistance.

Resistance measurements were performed using a Neilson Model 400 soil resistance meter operated in the two probe mode.

The proximity of the simulated anodes to the conductors and to one another resulted in an interference such that a correction of R_a was required. This was accomplished by measuring the resistance between two simulated anode rods as a function of their spacing and calculating from this the resistance of a single rod (R_a) at the requisite separation distance. All other components were removed from the test tank when this was done. Figure 11 shows the results of this as a plot of R_a versus separation distance. Thus, resistance of the rods increased with increasing separation distance and approached the value calculated using Equation 11 at a spacing beyond one

meter.* From Figure 11, R_a = 0.2185 Ω at 0.56 m. Next, this experiment was extended in order to determine a corrected resistance for the array of four simulated anodes. This involved replacing the simulated conductor array in Figure 9 with a fifth 12.7 mm rod. The measured resistance for this arrangement was 0.3625 Ω; and assuming the resistance of the central rod was 0.2185 Ω, the value for R_a (effective resistance of a single simulated anode in the four electrode array) was calculated as 0.151 Ω using Equation 14.

Next, an experiment was performed where the combined resistance of the simulated anode and conductor arrays (Figure 9) was measured for various array lengths by stepwise withdrawing the simulated conductors and anodes from the water. Figure 12 shows the results from this as a plot of the simulated conductor resistance which was calculated, on the one hand, using Equation 10 and, on the other, from the measured value and Equation 14. The resistance values which were determined from 1) experimental measurement and Equation 14 and 2) Equation 10 are seen to converge as electrode height increased and to be essentially the same beyond approximately 0.4 m. The increasingly large error as height diminished may have resulted from an increasingly large end effect at smaller heights. On the other hand, the resistance determined from surface area only (interference not considered) is less than the above by a factor of about seven. It is concluded that utilization of Equation 10 in conjunction with the protocol of progressively subdividing an electrode array into circular groupings (alternately, subgroups of four in a square arrangement) provides a technically viable means for calculating the resistance of conductor arrays on offshore structures.

---

* Resistance of the two electrodes increased to values greater than that indicated by Dwight's modified equation at separation distances beyond those shown here. This was attributed to interference from the test tank walls.

CONCLUSIONS

1. The slope parameter approach affords the same advantages to design of cathodic protection systems for conductor arrays as has been demonstrated previously for tubular structural members on offshore structures.

2. The resistance to ground of a square array of n conductors, where n/4 is a whole number, can be projected by 1) dividing the array into sub-groups of four conductors each, 2) calculating the resistance of each subgroup using the equation

$$R(n = 4) = \frac{1}{4}\left[R1(r) + 2\left[R1(D\sin(\pi/4))\right] + R1(D)\right],$$

where

$$R1(r_i) = \left[\frac{\rho}{2\pi L}\right]\left[\ln\left[\frac{L\left(1 + \sqrt{1 + (r/L)^2}\right)}{r}\right] + \frac{r}{L} - \sqrt{1 + (r/L)^2}\right],$$

electrode radius and length, respectively, 3) replacing the four electrodes of a subgroup with a centrally positioned single electrode of equivalent resistance, and 4) reapplying the above equation to the quadrapole of four, equivalent resistance electrodes.

3. Given the resistance of a conductor array, the design slope parameter can be calculated and an optimized cathodic protection and anode design (size, shape, and mass) projected. This represents an improvement over the present procedure which considers the conductor surface area but not the array resistance. However, even the slope parameter procedure does not assure that adequate protection is afforded to shielded areas of the array.

REFERENCES

1. "Corrosion Control of Steel-Fixed Offshore Platforms Associated with Petroleum Production", NACE Standard RP 0176-94, NACE International, Houston, 1994.

2. "Cathodic Protection Design", Recommended Practice RP B401, Det Norske Veritas Industri Norge AS, Hovik, Norway, 1993.

3. Foster, T. and Moores, V. G., "Cathodic Protection Current Demand of Various Alloys in Sea Water", Paper No. 295 presented at CORROSION/86, March 17-21, 1986, Houston.

4. Evans, S., "Use of Initial Current Density in Cathodic Protection Design", Material Performance, Vol. 27(2), 1988, p. 9.

5. Schrieber, C. F. and Reding, J., "Application Methods for Rapid Polarization of Offshore Structures", Paper No. 381, presented at CORROSION/90, April 23-27, 1990, Las Vegas.

6. Fischer, K. P., Sydberger, T., and Lye, R., "Field Testing of Deep Water Cathodic Protection on the Norwegian Continental Shelf", paper no. 67 presented as CORROSION/87, March 9-13, 1987, San Francisco.

7. Hartt, W. H., Culberson, C. H., and Smith, S. W., Corrosion, Vol. 40, 1984, p. 609.

8. Lin, H-S. and Dexter, S. C., Corrosion, Vol. 44, 1988, p. 615.

9. Finnegan, J. E. and Fischer, K. P., "Calcareous Deposits: Calcium and Magnesium Ion Concentrations", paper no. 581 presented at CORROSION/89, April 17-21, 1989, New Orleans.

10. Fischer, K. P. And Finnegan, J. E., "Cathodic Protection Behavior of Steel in Sea Water and the Protective Properties of the Calcareous Deposits", paper no. 582 presented at CORROSION/89, April 17-21, 1989, New Orleans.

11. Luo, J. S., Lee, R. U., Chen, T. Y., Hartt, W. H., and Smith, S. W., Corrosion, Vol. 47, 1991, p. 189.

11. Luo, J. S., Lee, R. U., Chen, T. Y., Hartt, W. H., and Smith, S. W., Corrosion, Vol. 47, 1991, p. 189.

12. Mantel, K. E., Hartt, W. H., and Chen, T. Y., Corrosion, Vol. 48, 1992, p. 489.

13. Wang, W., Hartt, W. H., and Chen, S., Corrosion, Vol. 52, 1996, p. 419.

14. Hartt, W. H., Chen, S., and Townley, D. W., "Sacrificial Anode Cathodic Polarization of Steel in Sea Water," paper no. 97474 presented at CORROSION/97, March 9-14, 1997, New Orleans.

15. Goolsby, A. D. and McGuire, D. P., "Cathodic Protection Upgrade of the 1,050' Water Depth Cognac Platform," paper no. 97472 presented at CORROSION/97, March 9-14, 1997, New Orleans.

16. Dwight, H. B., Electrical Engineering, Vol. 55, 1936, p. 1319.

17. Sunde, E. D., *Earth Conduction Effects in Transmission Systems*, Dover Publications, Inc., New York, 1968.

18. McCoy, Transactions Institute of Marine Engineers, Vol. 82, 1970, p. 210.

19. Cochran, J. C., "A Correlation of Anode-to-Electrolyte Resistance Equations Used in Cathodic Protection," paper no. 169 presented at CORROSION/82, March 22-26, 1982, Houston.

20. Strommen, R., Materials Performance, Vol. 24(3), 1985, p. 9.

21. Sunde, E. D., *Earth Conduction Effects in Transmission Systems*, Dover Publications, Inc., New York, 1968, p. 72.

22. Cochran, J. C., "Additional Anode-to-Electrolyte Resistance Equations Useful in Offshore Cathodic Protection," paper no. 254 presented at CORROSION/84, April 2-6, 1984, New Orleans.

FIGURE CAPTIONS

Figure 1: Schematic illustration of the initial dynamic polarization curve and the long-term potential-current density trend for galvanically polarized steel in sea water in perspective to four design slope parameter choices.

Figure 2: Schematic illustration of a four-by-four conductor array.

Figure 3: Schematic illustration of four identical, cylindrical electrodes equally spaced about a circle.

Figure 4: Schematic illustration of 16 identical, cylindrical electrodes equally spaced in a square array and representation of these in terms of four subgroups of four with each subgroup being replaced by a centrally positioned electrode of equivalent resistance.

Figure 5: Resistance of the aluminum anode array necessary to protect 16, 0.51 m diameter conductors as a function of water depth according to the NACE RP0176-94 procedure (1).

Figure 6: Resistance of a four-by-four array of 0.51 m diameter conductors with a centerline spacing of 2.29 m as a function of water depth, as determined from Equation 10.

Figure 7: Resistance of 1) the aluminum anode array (Figure 5), 2) the conductor array (Figure 6), and 3) the sum of these two resistances as a function of water depth.

Figure 8: Plot of potential versus current density showing the slope parameter design line where 1) anode resistance only was considered (RP0176) and 2) anode and conductor resistances were considered for water depths of 30, 100, and 300 m.

Figure 9: Schematic top and side views of the down-scaled, simulated conductor array and four symmetrically positioned anodes.

Figure 10: Equivalent electrical circuit for the simulated anode and conductor arrays in Figure 9.

Figure 11: Experimentally determined resistance of a single 12.7 mm diameter by 0.584 m long steel rod (one of the four simulated anodes in Figure 9) in sea water as a function of its separation distance from a second identical rod. Also shown is the rod resistance as calculated using Dwight's equation (Equation 11).

Figure 12: Resistance of the down-scaled, simulated conductor array 1) as determined experimentally and using Equation 14 and 2) as calculated from Equation 10.
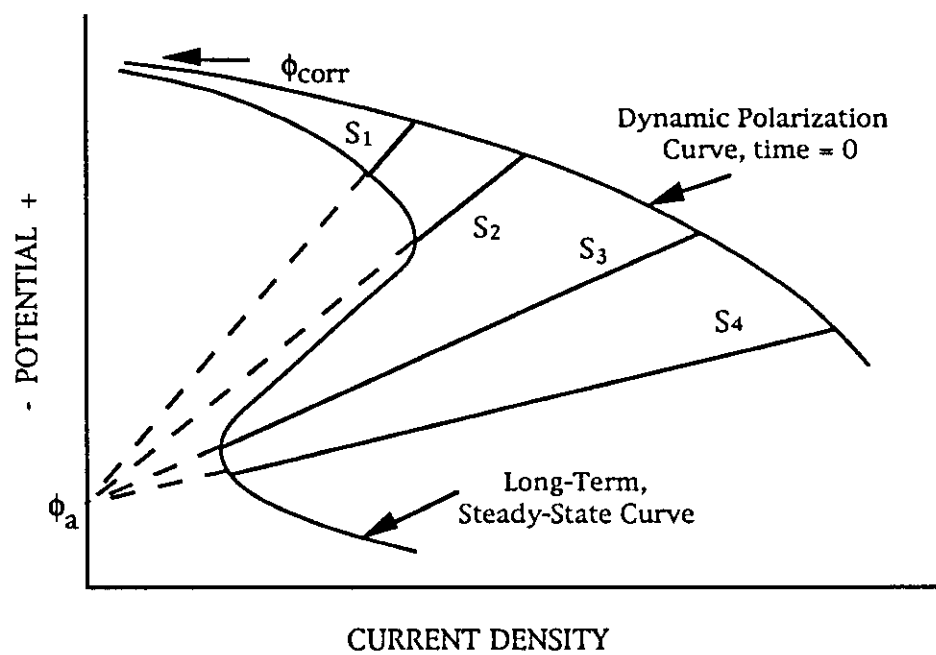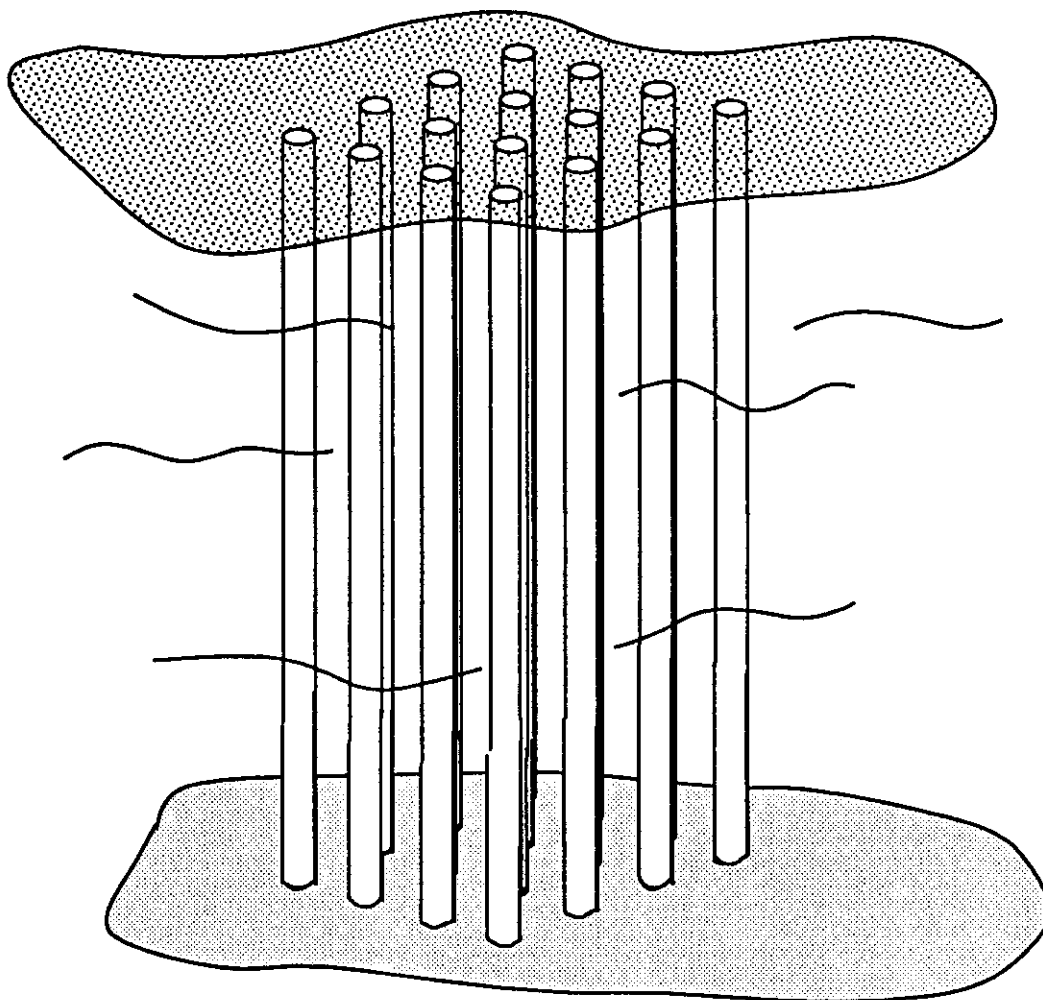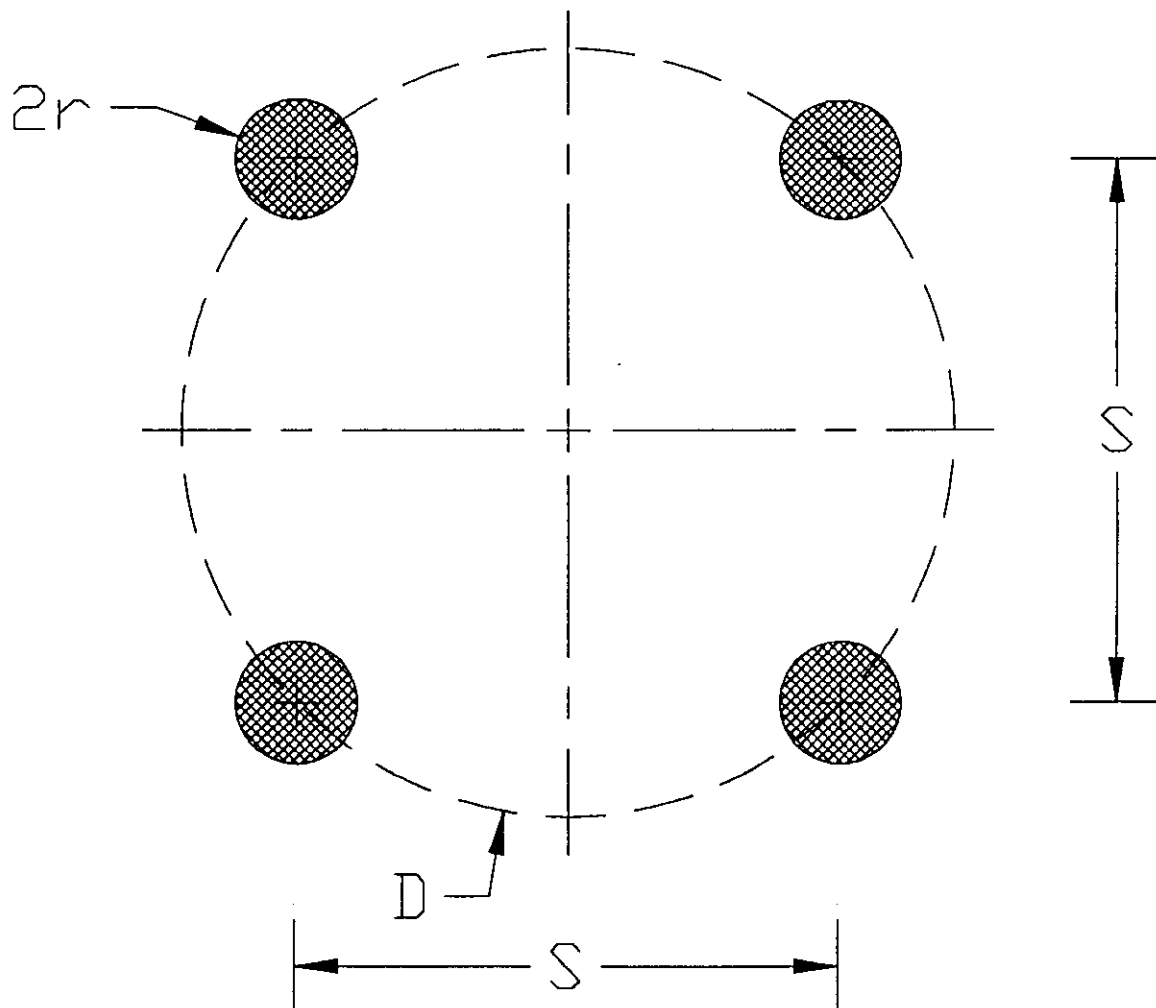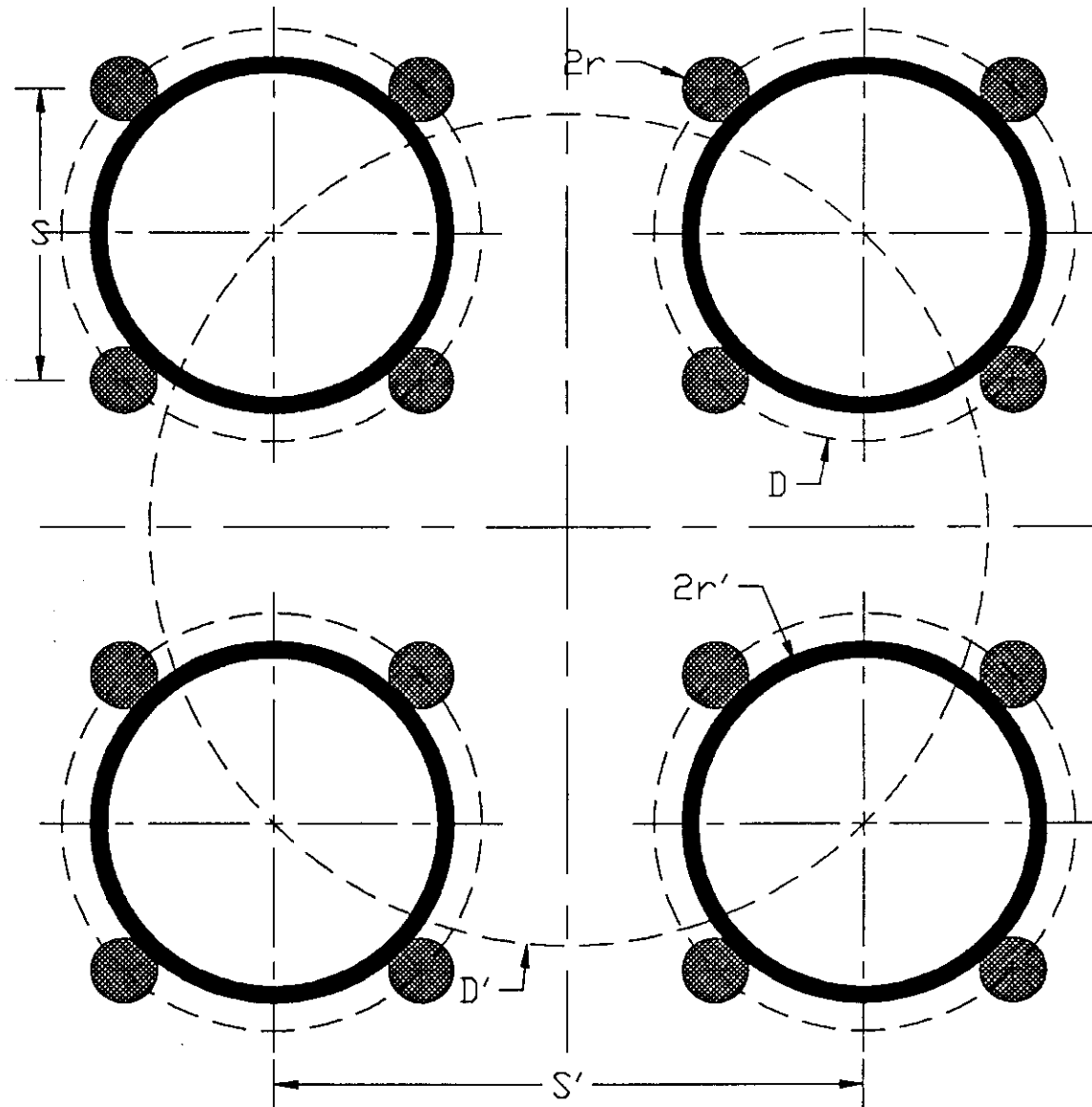
Figure 1

Figure 2

2r is the electrode diameter,
S is the spacing between any two adjacent electrodes,
D is the diameter of an imaginary circle, on the perimeter of which the four electrodes lie.

* All distances are taken center-to-center

Figure 3

2r is the individual electrode diameter,

D is the diameter of an imaginary circle, on the perimeter of which four of the original electrodes lie,

S is the spacing between any two adjacent electrodes,

2r' is the diameter of an equivalent resistance electrode,

D' is the diameter of an imaginary circle, on the perimeter of which four equivalent resistance electrodes lie,

S' is the spacing between adjacent equivalent resistance electrodes.

* All distances are taken center-to-center

Figure 4

Figure 5

Figure 6

16

Figure 7

Figure 8

12.7 mm dia.

I/4

ρ

0.56 m

I/4

0.584 m

16 electrodes,
3.18 mm dia.

3X 14.3 mm

SIDE VIEW

● R_a

ρ

I/4

I/4 R_c

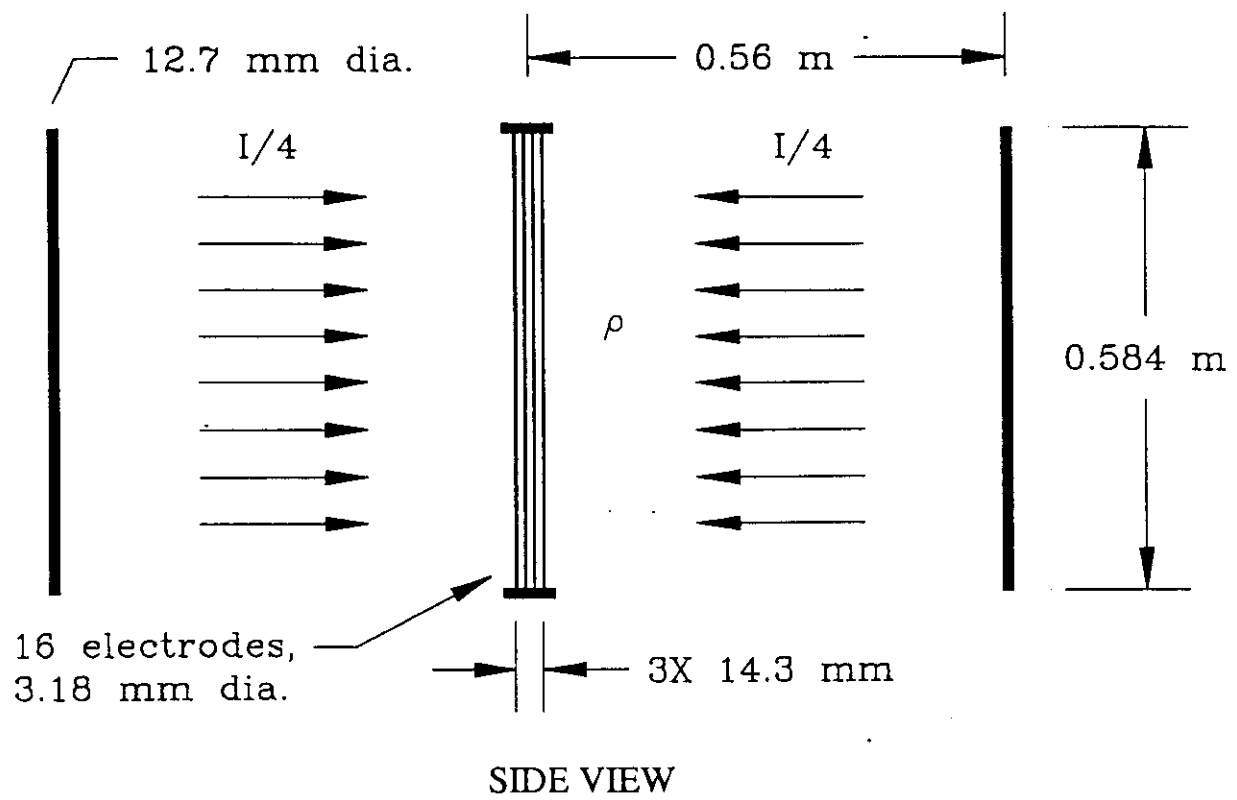● R_a ● R_a
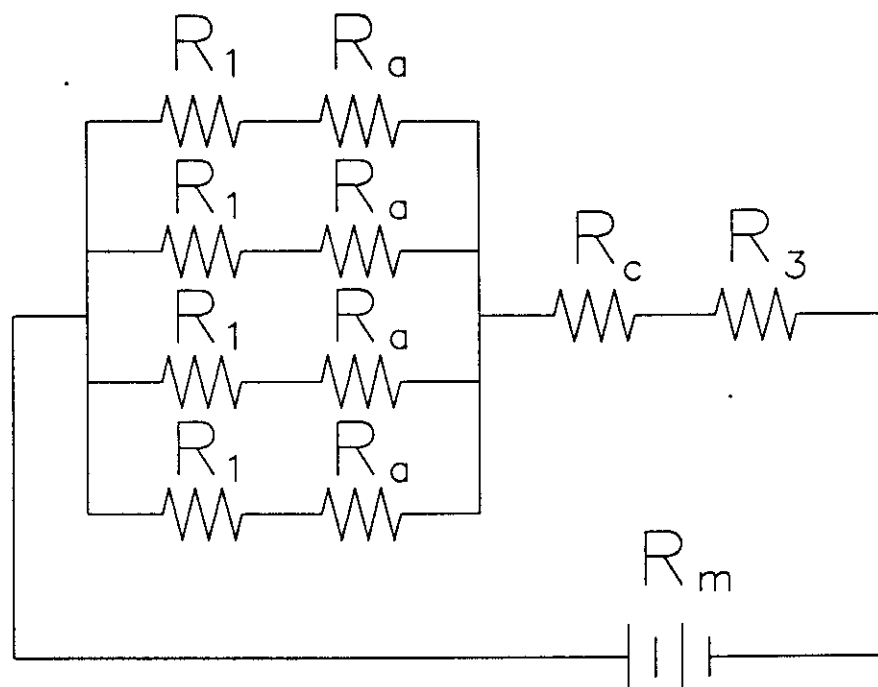
I/4

I/4
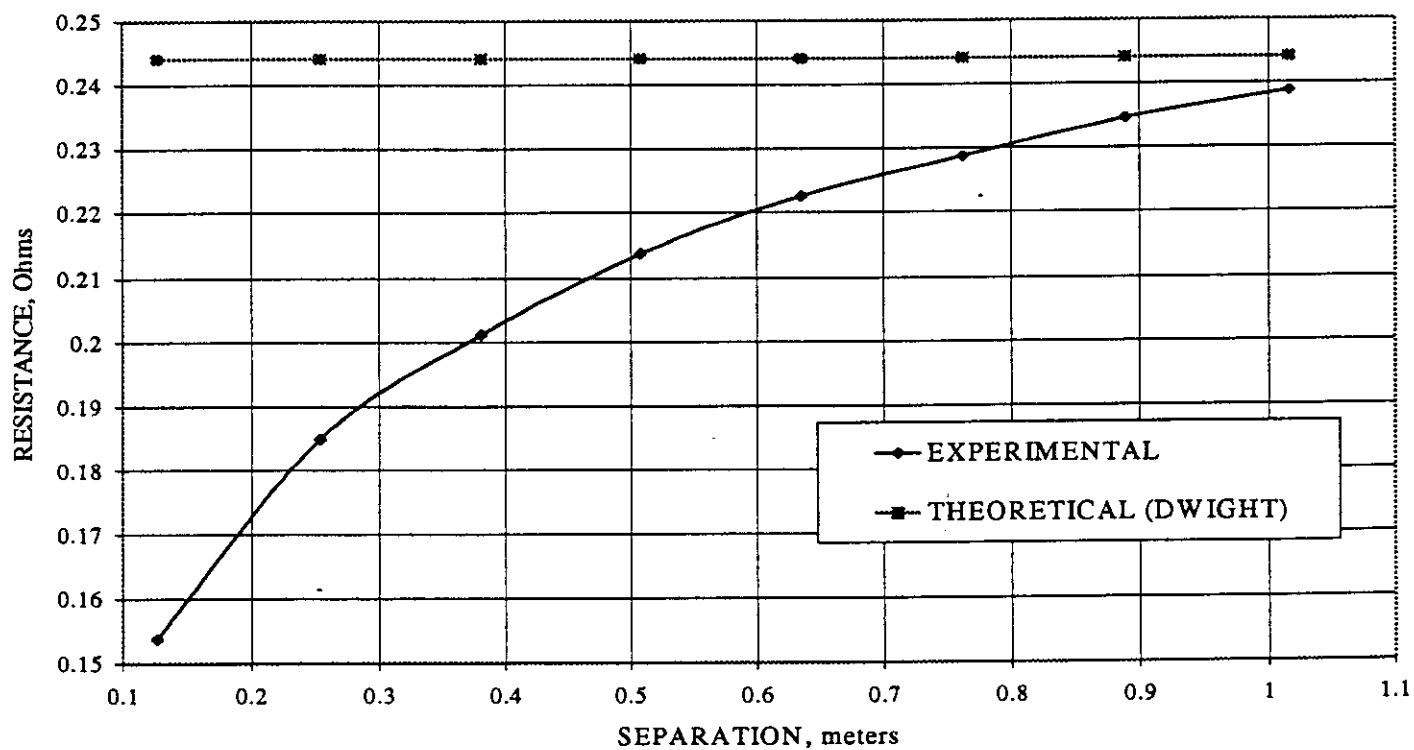
● R_a

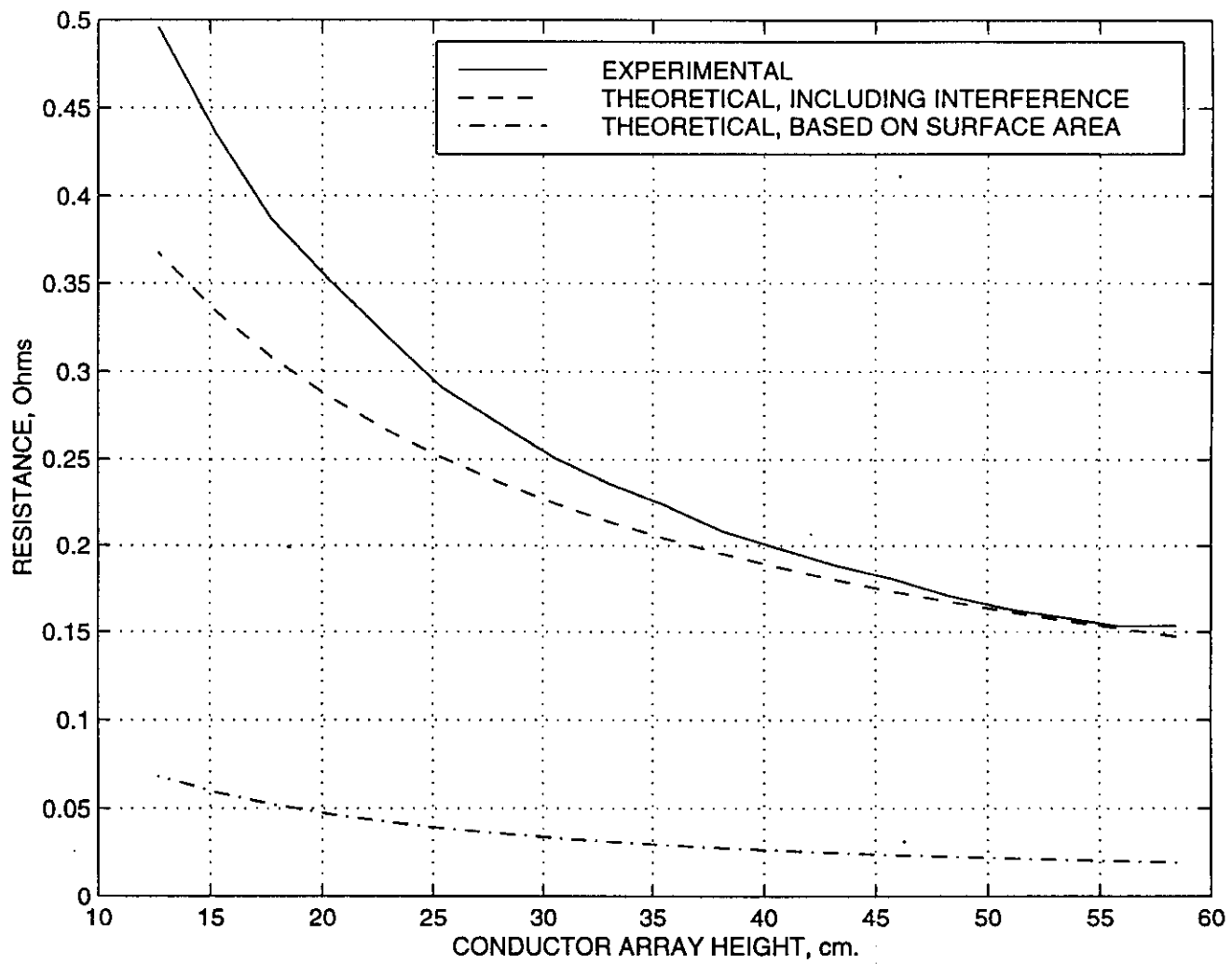TOP VIEW

Figure 9

19

Figure 10

Figure 11

20

Figure 12

21
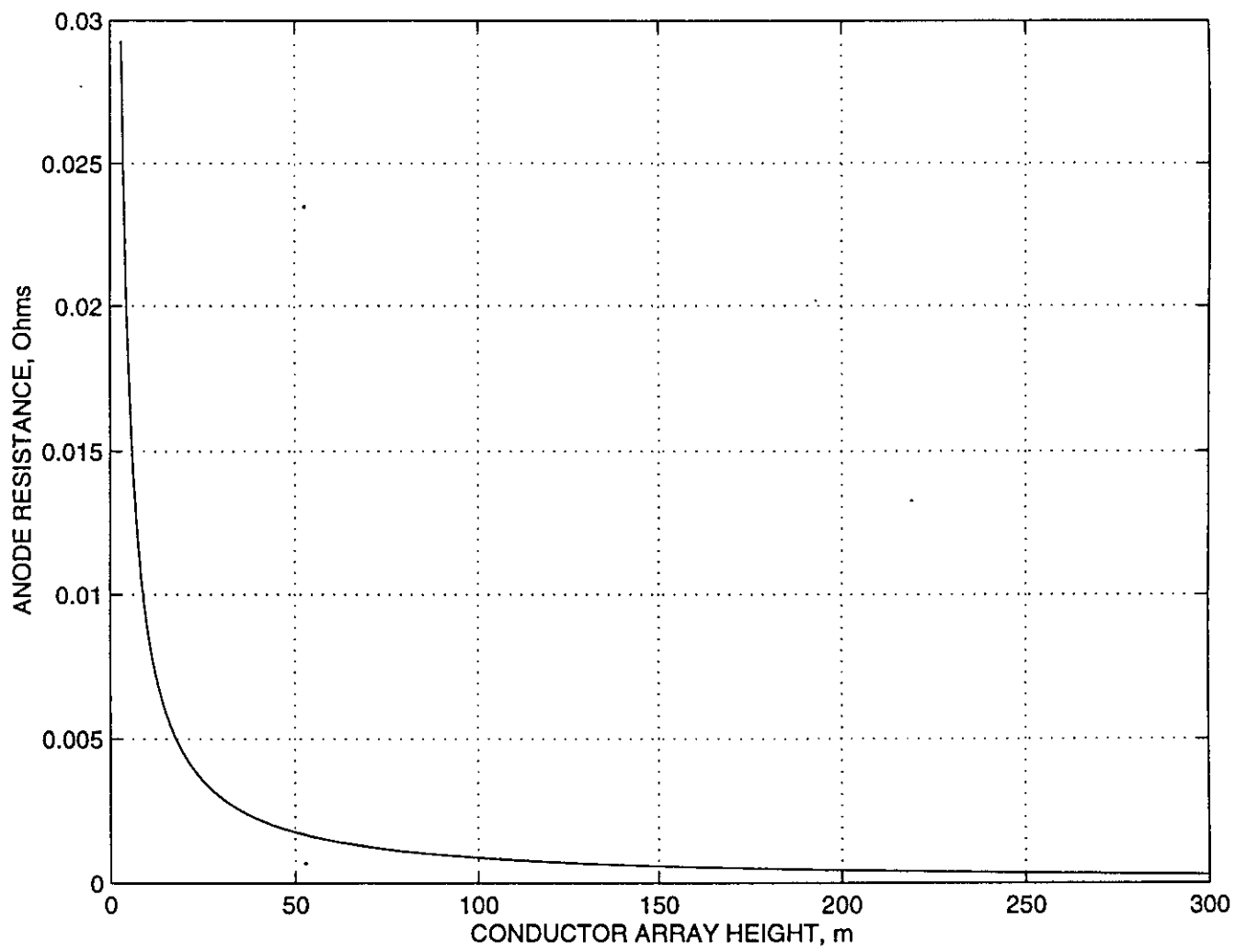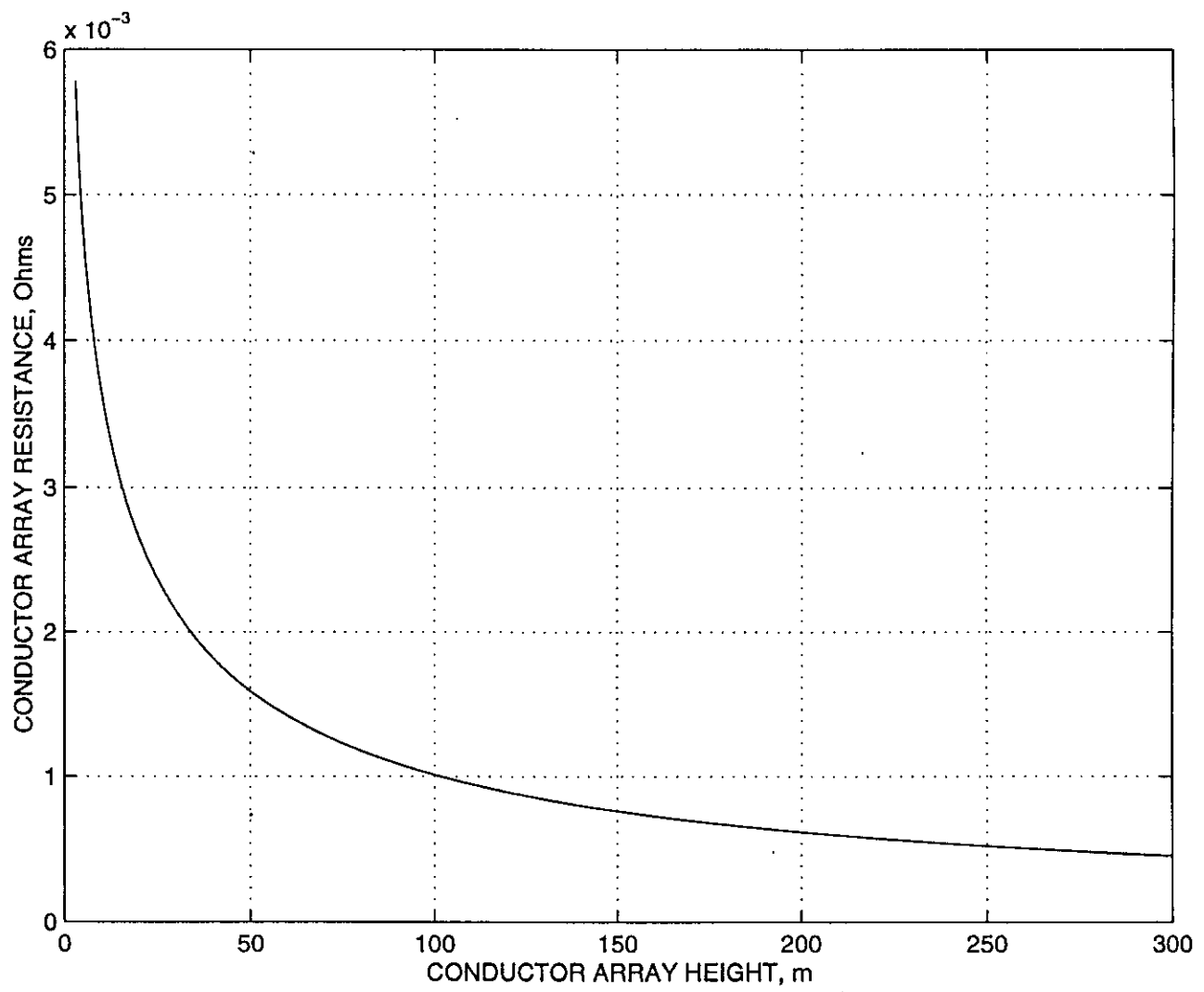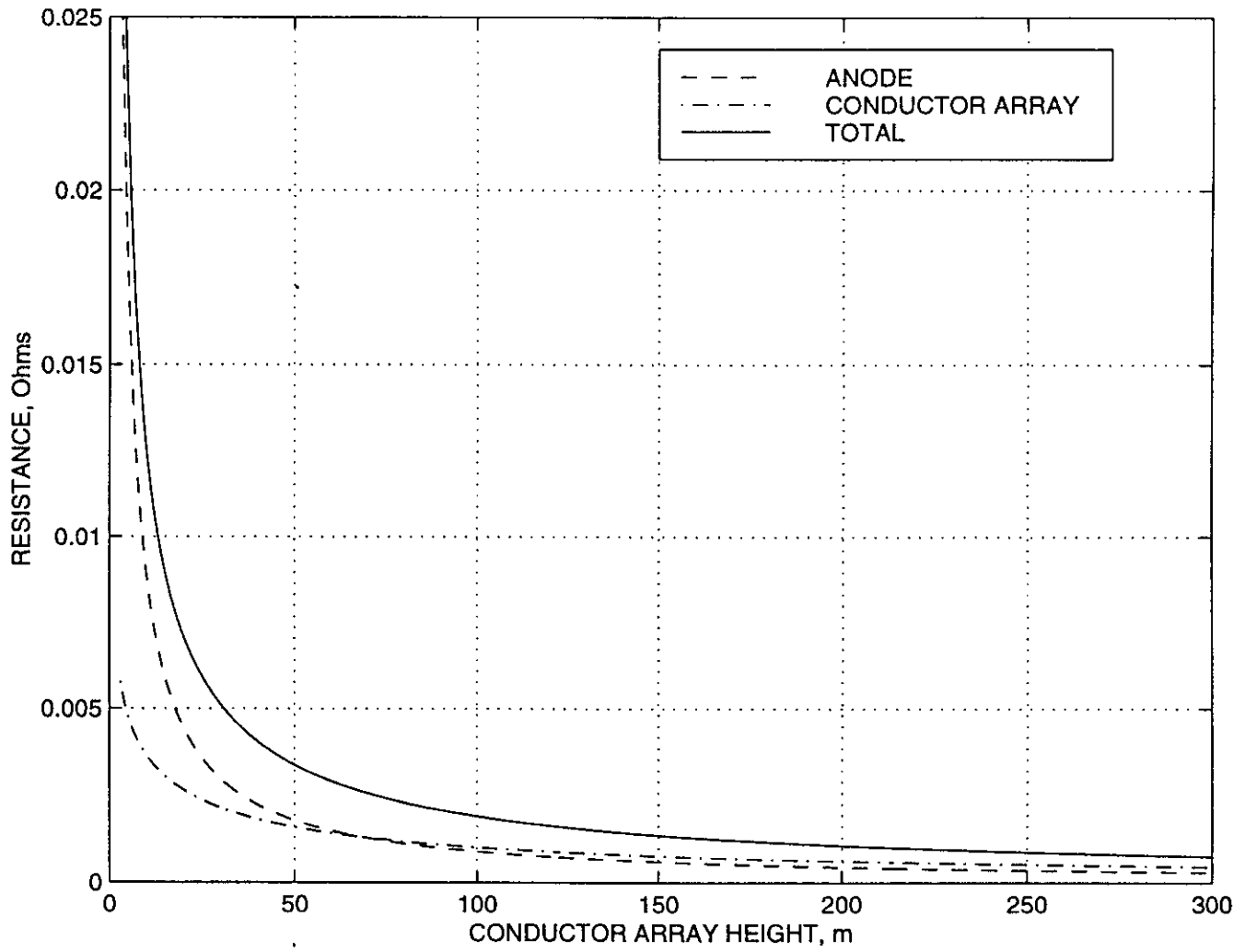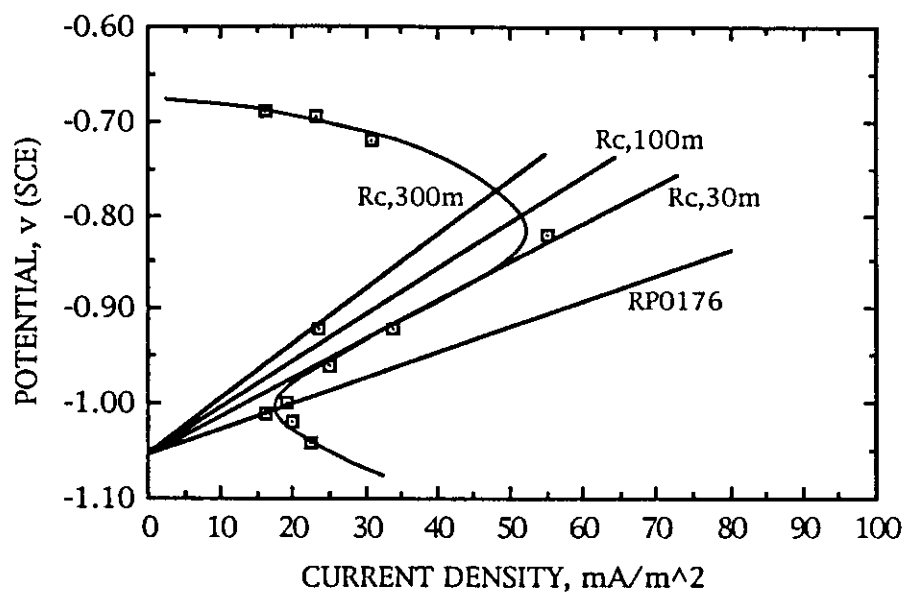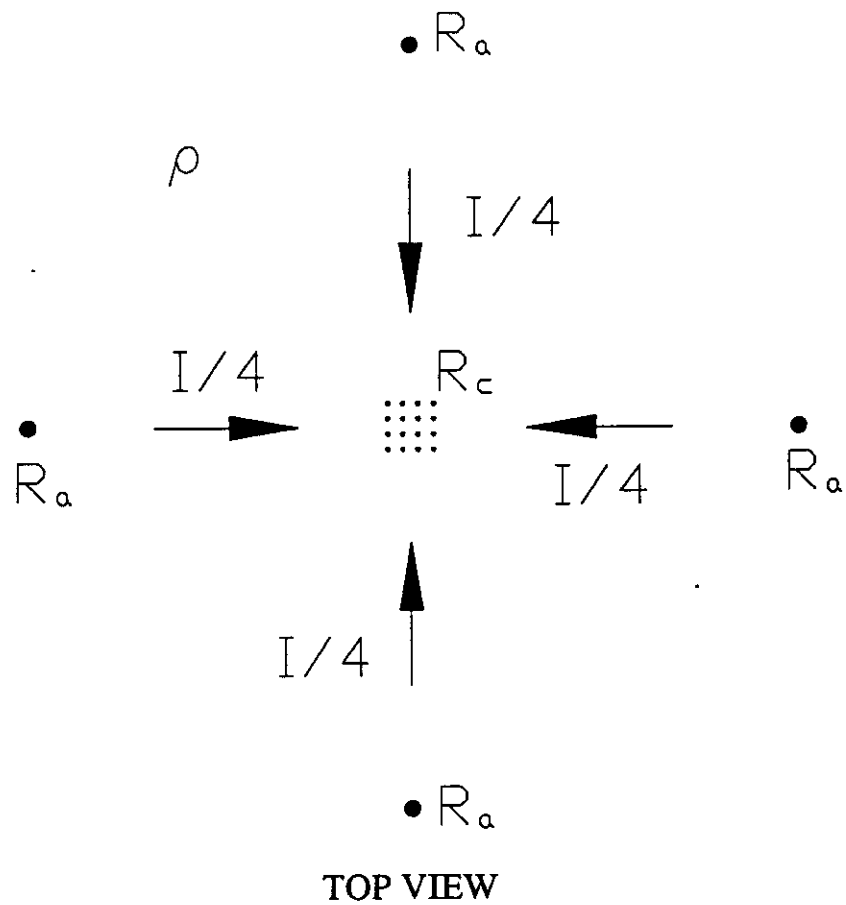
THE EFFECT OF VELOCITY UPON MAINTENANCE CURRENT DENSITY FOR CATHODICALLY POLARIZED STEEL IN SEA WATER

Dickson Hugus˙ and William H. Hartt
Center for Marine Materials
Department of Ocean Engineering
Florida Atlantic University
Boca Raton, Florida 33431

ABSTRACT

A series of cathodic polarization experiments was performed in which sections of UNS G10230 steel pipe were galvanically coupled through an external resistor to aluminum anode rings. These cells were incorporated into a sea water flow loop such that the hydrodynamic conditions were quantitatively defined. Sea water velocity for the experiments was 0.03, 0.09, and 0.30 m/s. From the results, the steady-state potential versus current density trend at a given velocity was characterized in terms of the recently proposed slope parameter approach to cathodic protection design. Also, an expression for the velocity dependence of the maintenance current density was developed. Anomalous behavior was encounter for some specimens tested at velocities of 0.09 and 0.30 m/s in that these exhibited a period of depolarization followed, in some cases, by repolarization. This behavior is discussed in terms of transitory calcareous deposit protectiveness, possibly reflecting the relative amounts of Ca and Mg in the deposits at a particular time.

INTRODUCTION

Cathodic protection, either with or without coatings, has served for decades as the corrosion control method of choice for steel members and structures in sea water. While in the past the incentives for optimizing this protection have been relatively modest, the advent of deep water petroleum production activities and environmental concerns have prompted research studies which have led to 1) design for rapid polarization (1-4), 2) an improved understanding of calcareous deposits and structure current demand (5-10), and 3) development of the slope parameter approach to cp design (11-13). Throughout these studies and the evolution of various design practices (14-16), the maintenance or mean current density, i_m; that is, the time average current density over the design life of the cathodic protection system, has remained a key parameter. This term is represented in the current design practices (15,16) by the relationship

/

$$i_m = \frac{N \cdot C}{A_c \cdot T},$$

$$(1$$

where

> N is the requisite number of anodes,
> C is anode current capacity,
> A_c is cathode surface area, and
> T is the design life.

In the slope parameter format (11-13), this expression becomes

$$i_m = \frac{R_a \cdot w \cdot C}{T \cdot S},$$

$$(2$$

where S is the slope parameter. With development of this latter equation, the design process was elevated from a procedure in which overdesign by some undetermined amount is implicit to one which is first principles based (12). Still to be developed, however, is an improved method for projecting i_m, since presently this is determined only by prior service experience in comparable ocean locations or by experiments and test exposures which simulate such experience. Even information which is developed from these may be inadequate or misleading, as evidenced by the fact that the existing recommended practice (15) lists the design mean current density for Gulf of Mexico as 55 mA/m² (5 mA/ft²), whereas long-term steady-state values an order of magnitude or more below this have been reported (17).

It is now well established from corrosion principles that cathodic protection current demand for a structure and, hence, i_m are governed by oxygen availability or by the rate of oxygen transport across the diffusional and hydrodynamic boundary layers, as affected by temperature, relative water movement (velocity), and surface films (coatings, calcareous deposits, and fouling). Particularly absent are studies which incorporate sea water velocity as a control variable; and, particularly, ones where this parameter has been characterized hydrodynamically. Exceptions include the research of Wolfson and Hartt (18), Smith et al. (19), and Gartland et al. (20), each of whom potentiostatically polarized steel specimens under controlled sea water flow conditions. However, the potentiostatic nature of these tests was such that, while information was gained regarding calcareous deposits and the capability for these to reduce current demand as exposure time progressed, the results are not quantitatively relatable to galvanic cathodic protection where both potential and current density change with time.

A procedure for addressing the combined influences of electrolyte flow and presence of calcareous deposits upon current density has been proposed based upon the Sherwood (Sh), Schmidt (Sc), and Reynolds (Re) numbers (19,20). Thus, for flow along a straight circular cross section pipe, the Reynolds number is expressed as

$$Re = \frac{v \cdot d}{\nu},$$

$$(3$$

where

> v is the average fluid velocity,
> d is inside pipe diameter, and
> v is kinematic viscosity.

Flow under these conditions is considered turbulent if the Reynolds number exceeds 2,100 and laminar at values less than this. The Schmidt number, on the other hand, characterizes the diffusional nature of the electrolyte according to

$$Sc = \frac{v}{D}.$$ (4

where D in the present case is the oxygen diffusivity. The Sherwood number is determined from

$$Sh = 0.03[Re]^{0.8} \cdot [Sc]^{0.33},$$ (5

and this can be incorporated into Fick's second law (21) such that

$$i_L = \frac{D \cdot n \cdot F \cdot c}{(x/Sh) + (t/p)},$$ (6

where

> i_L is the limiting current density for oxygen concentration polarization (equivalent to i_m),
> n and F have their normal meanings,
> c is the bulk dissolved oxygen concentration,
> x is average length of the pipe, and
> p is the porosity constant of the calcareous deposit (unitless).

In conjunction with development of the slope parameter approach to design of galvanic cathodic protection systems, an experimental methodology was developed which facilitates quantitative characterization of polarization in terms of field relevant parameters (11). The objective of the present research was to extend this approach to experiments where flow was controlled and quantified for the purpose of characterizing i_m in terms of both electrochemical and hydrodynamic parameters.

EXPERIMENTAL PROCEDURE

Materials. Anodes for the experiments were machined into a ring shape from an Al-Zn-Hg casting. The cathodes, on the other hand, were cylinders that were sectioned from a 3.7 m length of 10 cm (4 in) nominal diameter UNS G10230 steel pipe with the internal surface being polished to a 600 grit finish. Interior surface area of the steel cathodes was 506 cm^2 and for the anodes 43 cm^2, such that surface area ratio (anode-to-cathode) was 0.085. Both specimen types were degreased after preparation. Final dimensions were as shown in Figure 1; and chemical composition of the aluminum and steel is presented in Tables 1 and 2, respectively.

3

Test Cells and Test System. A schedule 80 pvc slip flange was compression fitted about each end of the steel cathode specimens, and the joint between the two was sealed at the outer surface. A machine screw was then soldered to the outer steel surface at the mid-length. Anode rings were drilled and tapped on the outside surface and fitted with a machine screw. In both cases, these screws served as sites for electrical connection.

Figure 2 shows the test cell configuration, which was comprised of 1) a steel cathode with flanges, 2) an aluminum anode ring, 3) a pvc pipe section with flanges, 4) an external resistor between the anode and cathode, and 5) a Ag/AgCl reference electrode. The external resistor was employed to affect a particular value for the slope parameter. The Ag/AgCl reference electrodes were fabricated from 0.5 mm diameter Ag wire and molten AgCl. These were potted in a threaded pvc cap using silicone and then positioned into a length of pvc pipe with end flanges of similar dimensions as for the steel cathode such that the tip of the reference electrode extended below the interior pvc pipe surface. Different sections were bolted together across an anode ring such that a water tight seal was affected. All components had the same internal diameter, and caution was taken to ensure that these aligned with one another.

Figure 3 schematically illustrates the test system that was employed for the first set of experiments (Set 1). This consisted of an upper reservoir tank which gravity fed sea water from an elevation of approximately two meters through three flow lines, each of which was inclined at a 22° angle. Each flow line consisted of four test cells (Figure 2) mounted in parallel. From the flow lines, the water emptied into a lower reservoir and was then pumped back to the upper reservoir.

Upon completing the first set of experiments and opening the system, it was determined that corrosion products from the anode had settled along the bottom of the line and that these extended onto the initial portion of the adjacent cathode. Also, corrosion products on the marginally protected and underprotected cathodes indicated that the flow had a spiral component, apparently because of the relatively short distance from the upstream ell to the test sections. Consequently, the test system was modified for the second set of tests (Set 2). This modification included 1) positioning the flow lines so that these were vertical, 2) adding 13 mm diameter pvc pipe sections within the pvc portion of the lines as flow straighteners, and 3) repositioning the anodes so that these were downstream, rather than upstream, from the corresponding cathode. Figure 4 shows a schematic illustration of this arrangement.

Flow rate was controlled by a gate valve in each line such that average velocities of 0.03, 0.09, and 0.30 m/s, as determined by flow volume per unit time measurements, were affected. The sea water was pumped continuously to the laboratory from a buried offshore wellpoint, and this has been shown by monitoring during an annual cycle to be typical of semi-tropical ocean water (22). In the flow system, this water was replenished at an exchange rate of five to six turnovers per day.

A Reynolds number calculation (Equation 3) indicated that flow in the 10 cm test line was turbulent at each of the three velocities. At the same time, flow in the flow straighteners that were added for Set 2 was laminar.

Consequently, this may have resulted in a laminar to turbulent flow transition along the steel cathode specimens in the Set 2 experiments.

External resistors were sized such that one specimen in each flow line had a slope parameter of 0.32, 0.63, 1.94, and 3.85 $\Omega \cdot m^2$ during Set 1 and 0.081, 0.17, 0.32, and 0.63 $\Omega \cdot m^2$ for Set 2. Cathode potential and voltage drop across the external resistors were monitored during the experiments and were recorded using a Keithly Metrabyte PC based data acquisition system.

RESULTS AND DISCUSSION

Polarization Data

Potential and current density for all specimens decreased during the initial 100 or so hours of exposure and approached steady-state values as illustrated by the example in Figure 5 which plots a) potential versus time, b) current density versus time, and c) potential versus current density (ϕ-i). This behavior is similar to what has been reported from similar galvanic cp experiments (11,12) and is attributed to progressive oxygen concentration polarization in conjunction with formation of calcareous deposits. Previous studies have shown this ϕ-i data trend (Figure 5c) to conform to the relationship

$$\phi_c = (R_t \cdot A_c)i_c + \phi_a,$$ (7

where

ϕ_c is the cathode potential,
R_t is total circuit resistance (dominated in the present case
    by magnitude of the external resistor), and
ϕ_a is the anode potential.

Thus, the ϕ-i trend is projected to be linear with slope $S = R_t \cdot A_c$ and with intersection of the vertical axis at ϕ_a provided S and ϕ_a are constant with time. The departure from linearity in Figure 5c probably reflects a period of anode activation during the initial stages of the test (upper right portion of the curve) and partial passivation of the anode once current density became low (lower left).

The above example where potential and current density decreased monotonically to steady-state values was termed normal behavior, as contrasted with exceptions to this which were also noted. Tables 3 and 4 list steady-state potentials for the test specimens in Set 1 and 2 experiments, respectively, and indicate that such exceptions to normal polarization occurred mostly at the highest velocity (0.30 m/s) and, to a lesser degree, at the intermediate velocity (0.09 m/s). All tests at the lowest velocity exhibited normal behavior. These occurrences of exceptional behavior were categorized according to:

Category 1: Cathode depolarization followed by repolarization (ϕ versus i
      linear),

Category 2: Cathode depolarization without subsequent repolarization (ϕ versus i linear), and

Category 3: Cathode depolarization followed by repolarization (ϕ versus i non-linear).

In addition, two types of Category 1 behavior were encountered. The first, which was designated as Type 1, occurred relatively early in the tests and was of short duration, while the second (Type 2) occurred later and lasted longer. Figures 6-8 illustrate examples of each category. Thus, in the case of Figure 6 two depolarization/repolarization events are noted, where the first (Category 1/Type 1) occurred in the 100-200 hours time frame and the second (Category 1/Type 2) at 500-2500 hours. Figure 7 shows an example where both Category 1/Type 1 and Category 2 behaviors occurred; and, lastly, Figure 8 shows an example of Category 3. The ϕ-i plots for the Categories 1 and 2 behavior (Figures 6 and 7) are essentially linear and, as such, indicate that both circuit resistance and ϕ_a remained constant throughout the experiments. Instances of Category 2 behavior were noted only in Set 1 experiments. Since the duration of these experiments was shorter than for Set 2 tests (1,850 compared to 4,500 hours), it is possible that Category 2 behavior was the same as for Category 3 but that there was insufficient time for repolarization in the former case. The non-linear trend in the case of Category 3, on the other hand, indicates that either R_t or ϕ_a (or both) changed (increased) as these experiments progressed. To investigate this, anode and cathode potentials (current-on values) were recorded periodically over a two week period; and the potential difference between these two (ϕ_c - ϕ_a) was determined and compared with the voltage drop across the external resistors. These results are shown in Table 5, which indicates that the magnitude of these two parameters was essentially the same. It was concluded from this that a circuit resistance increase, as could result from either corrosion product accumulation upon the anode or calcareous deposits upon the cathode, or a combination of these two, was not a factor and that polarization of the anode caused the ϕ-i non-linearity.

It is expected that the cathode is controlling with regard to current in experiments such as the present. That this was the case in instances of normal and Categories 1 and 2 behavior is indicated by the fact that current density tracked potential; that is, a positive potential excursion was accompanied by a current density increase and visa versa (see Figure 6 and 7). If this was the case, then some developmental aspect in the formation of the calcareous deposit, whereby its protectiveness was at first compromised and later restored, must have been responsible.

A similar trend as for Category 1/Type 1 and Category 2 behavior occurred also in Category 3 (Figure 8) to about 1,500 hours; but beyond this current density decreased with time while cathode potential remained about the same (slightly negative to -0.80 v) to about 2,850 hours and then increased to approximately -0.70 v. During this same period, ϕ_a increased to near this same value (-0.70 v). This trend, coupled with the fact that the peak current density upon the anode (1,500 hours into the test) was 10 A/m^2, suggests that the critical current density may have been reached and that the anode partially passivated.

In evaluating data for the various specimens, consideration was given to the fact that the experimental setup was changed between the Set 1 and Set 2

tests, as explained in the preceding section. However, no distinctions in the potential-current density-velocity trends between the two sets were apparent; and so the data were analyzed assuming they conformed to a common population.

Velocity Dependence of Polarization

Figure 9 shows the ϕ-i data for each of the three velocities in cases where steady-state was achieved. Also included are results from previous tests (11) that were performed in a two liter test cell with a sea water exchange rate of 150 ml/min, for which velocity was considered "quiescent." The three Set 2 specimens for which the ϕ-i behavior was non-linear (Table 4) were not included in Figure 9 because steady-state was not achieved for these. In each case a trend curve has been added. Thus, the quiescent velocity data exhibited a relatively well defined sigmoidal trend. The 0.03 and 0.09 m/s data are displaced progressively toward higher velocity but show a trend similar to that of the quiescent curve, although scatter was greater and there are gaps in the data for the two higher velocities. The 0.30 m/s results, on the other hand, indicate a progressive current density increase as steady-state potential became more negative.

The maximum steady-state current density at the lower two velocities (quiescent and 0.03 m/s) occurred near -0.80 v (that this was so is less apparent in the 0.03 m/s case), whereas this maximum was at about -0.90 v for 0.09 m/s and at an even lower potential, assuming such a peak occurred at all, for 0.30 m/s. Such a trend (potential at which the peak current density occurred decreasing with increasing velocity above 0.03 m/s) indicates that rapid polarization and achievement of a low maintenance current density may become more difficult, if not impossible, at higher velocities.

The data in Figure 9 indicate that some specimens tested at different velocities developed approximately the same steady-state potential, namely -0.78, -0.88, and -0.98 v. This facilitated projection of a steady-state current density versus velocity relationship, as shown in Figure 10. In doing this, the quiescent water movement data (11) were assigned zero velocity. In a general sense, the data conform to a common, linear trend according to

$$i_m = 852v + 48. \tag{8}$$

On this basis, an order of magnitude increase in velocity caused about a four-fold increase in current density.

Calcareous Deposit Properties

Porosity. An attempt was made to evaluate the calcareous deposit porosity constant, p, in the equation

$$i_L = \frac{D \cdot n \cdot F \cdot c}{(x/Sh) + (t/p)}. \tag{6}$$

To accomplish this, the Reynolds number was determined for the present experimental setup assuming $v = 8.81 \cdot 10^{-7}$ m^2/s and the Schmidt number (Equation 4) assuming an oxygen diffusivity, D, of $2.72 \cdot 10^{-5}$ cm^2/s. From these,

the Sherwood number (Equation 5) was calculated based upon a bulk oxygen concentration, c, of 5 mg/l. Deposit thickness values were taken from previous research (18) for velocities and potentials that were comparable to those of the present test conditions, and the current densities (i_L) were those measured in this study. Table 6 lists these deposit thicknesses; and, accordingly, Table 7 indicates the calculated p values. Although the results are limited, they indicate that porosity increased with increasing velocity and with decreasing potential. Also, the ratio of deposit thickness-to-porosity was 3.3-5.7 times greater than the average pipe length-to-Sherwood number ratio. This indicates that the resistance to diffusion afforded by the calcareous deposit was of greater significance than that of the boundary layer.

Composition and Morphology. Following the experiments, one specimen from each flow line of Set 1 and all Set 2 specimens were analyzed by scanning electron microscopy and EDX. Specimens in the former case (Set 1) were selected such that steady-state potential was approximately the same for each. Figures 11-13 illustrate the morphology for these, where for the first (Figure 11, specimen no. I-194/03) the deposit was relatively coarse, with EDX indicating this was predominantly Ca. Figure 12, on the other hand, shows the morphology for specimen number I-63/09 and that this exhibited an inner deposit similar to that in Figure 11 and a finer grain outer one. EDX revealed the former to be calcium rich and the latter predominantly magnesium. Lastly, Figure 13 shows the deposit for specimen I-63/30 which was mostly fine grain and Mg rich. These micrographs suggest that there was a tendency for deposits which formed under these conditions (steady state potential approximately -0.98 v) to transition from Ca to Mg rich with increasing velocity. The calcium rich deposits were presumably aragonite ($CaCO_3$) and the magnesium ones brucite ($Mg(OH)_2$).

Set 2 specimens tested at 0.03 m/s velocity all polarized to -1.04 or -1.05 v, irrespective of slope parameter (see Table 4). Figure 14 illustrates the deposit morphology for specimen number II-17/03 and reveals this to be similar to what has been reported historically for comparable test conditions (5,9,10). EDX showed the composition to be Ca rich with only a trace of Mg. The deposits for other Set 2 specimens tested at this same velocity were similar to this with regard to both morphology and composition.

Steady-state potentials for Set 2, 0.09 m/s velocity specimens were in the range -0.96 to -0.99 v. An example of these for specimen number II-63/09 is shown in Figure 15. Here the morphology was a mixture of coarse and fine grain particles, which appear similar to those for specimen number I-63/09 (Figure 12); however, EDX showed both of these to be predominantly Ca.

Set 2 specimens tested at 0.30 m/s velocity exhibited a relatively broad range of steady-state potentials (Table 4) due to the fact that some of these depolarized and others did not, as described above. In this regard, specimen numbers II-081/30 and II-17/30 had final potentials that were positive to -0.70 v; and, consistent with this, relatively little calcareous deposit was present. Figure 16 shows examples of the deposit morphology on the other two specimens (specimen numbers II-32/30 and II-63/30) and that these also were a mixture of coarse and fine grain particles. EDX revealed these to be Ca rich.

Previous studies of calcareous deposits have ascribed significance to the relative amounts of Ca and Mg, which has often been characterized in terms the Ca-to-Mg ratio or Ca/Mg (23). Apparently, the Ca rich phase (either aragonite or calcite) serves as a more resistant barrier to oxygen diffusion than does the magnesium one (brucite). Because of gaps in the polarization data and because deposit compositional information was available for only two exposure times, it is not possible to construct a comprehensive evolutionary model of the calcareous deposits and to interrelate this to the potential-current density history. However, the depolarization and depolarization/repolarization trends in Figure 6-8, coupled with the finding that Ca/Mg was often low after 1,850 hours but high at 4,500 hours, suggests that, subsequent to initial rapid polarization, $Mg(OH)_2$ precipitated in some cases upon specimens exposed to the higher velocities and caused current demand for these to increase which resulted in depolarization. Subject to the anode potential remaining sufficiently negative, these specimens subsequently repolarized in response to $CaCO_3$ being reestablished as the principle deposit phase. The cause of such a velocity dependent deposit compositional cycle is undetermined. Also unclear is why such a cycle has apparently not been evident from data acquired in conjunction with monitoring programs on offshore structures for locations where water movements were comparable to those employed in the present study. A possible explanation for this is that biofouling, which was not present in these laboratory experiments since the sea water was filtered, may provide an additional barrier to water movement such that the effective velocity at the steel surface was lower than it would have been otherwise.

CONCLUSIONS

The following conclusions were reached based upon experiments where steel pipe sections were cathodically polarized galvanically in a sea water flow line at velocities of 0.03, 0.09, and 0.30 m/s and with slope parameters in the range 0.081-3.85 $\Omega \cdot m^2$:

1. In most cases polarization conformed to what was termed a normal trend where potential and current density decreased with time to a steady-state value. Exceptions were noted at the two higher velocities, however, where the initial polarization was followed by depolarization and, in some cases, repolarization. Apparently, some aspect of the higher flow rates caused the calcareous deposits to become less protective for some period and for current demand to increase.

2. The potential versus current density trend at the two lower velocities revealed a sigmoidal curve with a peak current density being achieved for 0.03 m/s tests at about -0.80 v (Ag/AgCl) and for 0.09 m/s at about -0.90 v. At the highest velocity (0.30 m/s), current density increased with decreasing potential for the entire range of slope parameters for which results were available.

3. For specimens which reached steady-state potentials in the range -0.78 to -0.98, the steady-state current density, i_m, increased with velocity, v, according to the expression

$$i_m = 852v + 48,$$

where units for current density are mA/m^2 and for velocity m/s.

4. Based upon thickness values taken from the literature, the deposit porosity constant was calculated to be in the range 0.035 to 0.104 (unitless).

5. For Set 1 specimens (exposure time 1,850 hours) tested at the two higher velocities (0.03 and 0.09 m/s), the calcareous deposit was comprised of a Mg rich, as well as a Ca rich, phase. In the case of Set 2 specimens (exposure time 4,500 hours), the deposit was Ca rich with only trace amounts of Mg. The depolarization/repolarization behavior that was noted may have been related to an evolutionary compositional aspect of calcareous deposit development where the relative amounts of Ca and Mg varied with time.

ACKNOWLEDGMENTS

REFERENCES

1. Foster, T. and Moores, V. G., "Cathodic Protection Current Demand of Various Alloys in Sea Water", Paper No. 295 presented at CORROSION/86, March 17-21, 1986, Houston.

2. Evans, S., "Use of Initial Current Density in Cathodic Protection Design", Material Performance, Vol. 27(2), 1988, p. 9.

3. Schrieber, C. F. and Reding, J., "Application Methods for Rapid Polarization of Offshore Structures", Paper No. 381, presented at CORROSION/90, April 23-27, 1990, Las Vegas.

4. Fischer, K. P., Sydberger, T., and Lye, R., "Field Testing of Deep Water Cathodic Protection on the Norwegian Continental Shelf", paper no. 67 presented as CORROSION/87, March 9-13, 1987, San Francisco.

5. Hartt, W. H., Culberson, C. H., and Smith, S. W., Corrosion, Vol. 40, 1984, p. 609.

6. Lin, H-S. and Dexter, S. C., Corrosion, Vol. 44, 1988, p. 615.

7. Finnegan, J. E. and Fischer, K. P., "Calcareous Deposits: Calcium and Magnesium Ion Concentrations", paper no. 581 presented at CORROSION/89, April 17-21, 1989, New Orleans.

8. Fischer, K. P. And Finnegan, J. E., "Cathodic Protection Behavior of Steel in Sea Water and the Protective Properties of the Calcareous Deposits", paper no. 582 presented at CORROSION/89, April 17-21, 1989, New Orleans.

9. Luo, J. S., Lee, R. U., Chen, T. Y., Hartt, W. H., and Smith, S. W., Corrosion, Vol. 47, 1991, p. 189.

10. Mantel, K. E., Hartt, W. H., and Chen, T. Y., Corrosion, Vol. 48, 1992, p. 489.

11. Wang, W., Hartt, W. H., and Chen, S., Corrosion, Vol. 52, 1996, p. 419.

12. Hartt, W. H., Chen, S., and Townley, D. W., "Sacrificial Anode Cathodic Polarization of Steel in Sea Water," paper no. 97474 presented at CORROSION/97, March 9-14, 1997, New Orleans. To be published in Corrosion.

13. D. W. Townley, "Unified Design Equation for Offshore Cathodic Protection," paper no. 97473 presented at CORROSION/97, March 9-14, 1997, New Orleans.

14. "Corrosion Control of Steel-Fixed Offshore Platforms Associated with Petroleum Production", NACE Standard RP 0176-76, NACE International, Houston, 1976.

15. "Corrosion Control of Steel-Fixed Offshore Platforms Associated with Petroleum Production", NACE Standard RP 0176-94, NACE International, Houston, 1994.

16. "Cathodic Protection Design", Recommended Practice RP B401, Det Norske Veritas Industri Norge AS, Hovik, Norway, 1993.

17. M. W. Mateer and K. J. Kennelley, "Design of Platform Anode Retrofits Using Measured Structure Current Density," paper no 526 presented at CORROSION/93, MARCH 8-12, 1993, New Orleans.

18. S. L. Wolfson and W. H. Hartt, Corrosion, Vol. 37, 1981, p. 70.

19. S. W. Smith, K. M. McCabe, and D. W. Black, Corrosion, Vol. 45, 1989, p. 790.

20. P. O. Gartland, E. Bardal, R. E. Andersen, and R. Johnsen, Corrosion, Vol. 40, 1984, p. 127.

21. T. K. Ross and D. H. Jones, J. Applied Chemistry, Vol. 12, 1962, p. 314.

22. W. H. Hartt, "Fatigue of Welded Structural Steel in Sea Water," paper no. 3982, Proceedings Offshore Technology Conference, Houston, May, 1981.

23. R. A. Humble, "Corrosion, Vol. 4, 1948, p. 358.

TABLE CAPTIONS

Table 1. Chemical composition of the aluminum anode material.

Table 2. Chemical composition of the steel cathode pipe material.

Table 3. Steady-state potentials for the steel cathodes specimens in Set 1.

Table 4. Steady-state potentials for the steel cathodes specimens in Set 2.

Table 5. Comparison of $\phi_c - \phi_a$ (anode-to-cathode potential difference) and voltage drop across the external resistors for Set 2 specimens.

Table 6. Calcareous deposit thickness at different potentials and velocities (18).

Table 7. Calculated values for calcareous deposit porosity.

FIGURE CAPTIONS

Figure 1. Schematic illustration of (a) a steel cathode specimen and (b) a n aluminum anode specimen after machining.

Figure 2. Schematic side view representation of the test cell layout.

Figure 3. Schematic side view rendering of the first experimental setup.

Figure 4. Schematic side view illustration of the second experimental setup.

Figure 5. Plot of (a) potential versus time, (b) current density versus time, and (c) potential versus current density for specimen number I-32/03 (slope parameter 0.32 Ω.m^2 and velocity 0.03 m/s).

Figure 6. Plot of (a) potential versus time, (b) current density versus time, and (c) potential versus current density for specimen number II-63/09 (slope parameter 0.63 Ω.m^2 and velocity 0.09 m/s).

Figure 7. Plot of (a) potential versus time, (b) current density versus time, and (c) potential versus current density for specimen number I-63/30 (slope parameter 0.63 Ω.m^2 and velocity 0.30 m/s).

Figure 8. Plot of (a) potential versus time, (b) current density versus time, and (c) potential versus current density for specimen number II-081/30 (slope parameter 0.081 Ω.m^2 and velocity 0.30 m/s).

Figure 9. Plot of steady-state potential versus steady-state current density for specimens of the present tests.

Figure 10. Plot of steady state current density as a function of velocity.

Figure 11: Scanning electron micrographs of the calcareous deposit which formed upon specimen number I-194/03 (S = 1.94 Ω . m^2 and v = 0.03 m/s).

Figure 12: Scanning electron micrographs of the calcareous deposit which formed upon specimen number I-32/09 (S = 0.32 Ω . m^2 and v = 0.09 m/s).

Figure 13: Scanning electron micrographs of the calcareous deposit which formed upon specimen number I-63/03 (S = 0.63 Ω . m^2 and v = 0.30 m/s).

Figure 14: Scanning electron micrographs of the calcareous deposit which formed upon specimen number II-17/03 (S = 0.17 Ω . m^2 and v = 0.03 m/s).

Figure 15: Scanning electron micrographs of the calcareous deposit which formed upon specimen number II-63/09 (S = 0.63 Ω . m^2 and v = 0.09 m/s).

Figure 16: Scanning electron micrographs of the calcareous deposit which formed upon a) specimen number II-63/03 (S = 0.63 Ω . m^2 and v = 0.30 m/s) and b) specimen number II-32/30 (S = 0.32 Ω . m^2 and v = 0.30 m/s).

Table 1

ELEMENT	COMPOSITION, w/o
Zn	1.444
In	<.0010
Hg	0.0433
Si	0.036
Cu	0.00345
Fe	0.038
Cd	0.0016
B	>0.03
Sn	0.0033
Mg	0.0075
Cr	0.002
Ni	0.0025
Mn	0.004
Ti	0.003
V	0.003
Bi	0.0023
Al	bal.

Table 2

ELEMENT	COMPOSITION, w/o
C	0.23
Mn	0.39
Si	0.04
Ni	0.01
Cr	0.03
Mo	<0.01
S	0.011
P	0.008
Cu	0.02

Table 3

SPECIMEN NUMBER	SLOPE PARAMETER, Ω-m^2	VELOCITY, m/s	STEADY-STATE POTENTIAL, v (Ag/AgCl)
I-32/03		0.03	-1.04
I-32/09	0.32	0.09	-0.98
I-32/30		0.30	** -0.88
I-63/03		0.03	-1.00
I-63/09	0.63	0.09	-0.90
I-63/30		0.30	** -0.84
I-194/03		0.03	-0.89
I-194/09	1.94	0.09	*1,** -0.78
I-194/30		0.30	*1 -0.67
I-385/03		0.03	-0.71
I-385/09	3.85	0.09	*1 -0.68
I-385/30		0.30	-0.66

*1: Exception 1, Type 1 (see Text for explanation).
**: Exception 2 (see Text for explanation).

Table 4

SPECIMEN NUMBER	SLOPE PARAMETER, Ω-m^2	VELOCITY, m/s	STEADY-STATE POTENTIAL, v (Ag/AgCl)
II-081/03		0.03	-1.05
II-081/09	0.081	0.09	-0.98
II-081/30		0.30	***
II-17/03		0.03	-1.04
II-17/09	0.17	0.09	-0.99
II-17/30		0.30	*1,***
II-32/03		0.03	-1.05
II-32/09	0.32	0.09	*2 -0.96
II-32/30		0.30	*1,***
II-63/03		0.03	-1.04
II-63/09	0.63	0.09	*1,*2 -0.97
II-63/30		0.30	*1 -0.78

Note: Where no potential is listed, specimen did not reach steady-state.
*1: Exception 1, Type 1 (see test for explanation).
*2: Exception 1, Type 2 (see test for explanation).
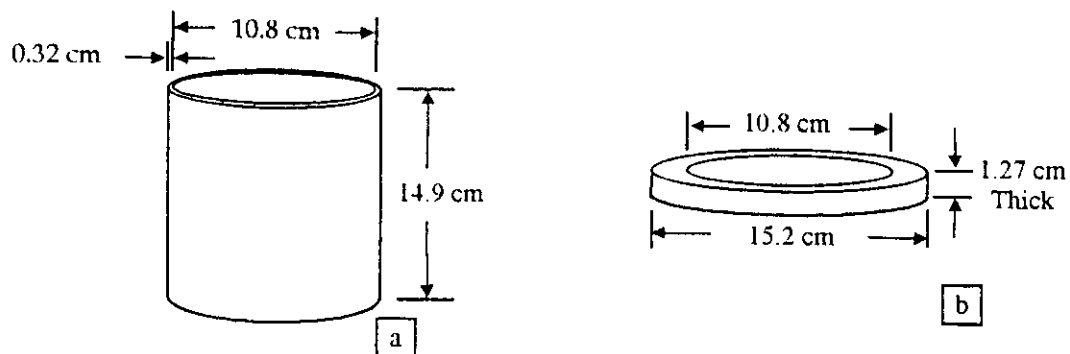***: Exception 3 (see text for explanation).

Table 5

SLOPE PARAMETER, Ωm^2	TIME, hrs	CATHODE POT., φc, v.	ANODE POT., φa, v.	φc - φa, v.	ΔV ACROSS RESISTOR, v
0.081	3,740	-0.689	-0.700	0.011	0.011
	3,915	-0.709	-0.720	0.011	0.011
	4,035	-0.695	-0.707	0.012	0.012
	4,165	-0.695	-0.706	0.010	0.011
0.17	3,740	-0.669	-0.691	0.022	0.021
	3,915	-0.673	-0.693	0.020	0.020
	4,035	-0.671	-0.689	0.018	0.019
	4,165	-0.67	-0.687	0.017	0.016
0.32	3,740	-0.832	-0.952	0.120	0.119
	3,915	-0.796	-0.926	0.130	0.130
	4,035	-0.775	-0.900	0.125	0.125
	4,165	-0.777	-0.897	0.120	0.119

Table 6

SEA WATER VELOCITY, m/s	POTENTIAL, v (SCE)	DEPOSIT THICKNESS, mm
0.30	-1.03	0.18
	-0.93	0.07
	-0.78	0.04
0.08	-1.03	0.06
	-0.93	0.05
	-0.78	0.03

Table 7

POTENTIAL (approximate) v, (Ag/AgCl)	PORO SITY (unit less)	
	0.09 m/s	0.30 m/s
-0.78	0.035	0.061
-0.89	0.086	0.104

Table 1

ELEMENT	COMPOSITION, w/o
Zn	1.444
In	<.0010
Hg	0.0433
Si	0.036
Cu	0.00345
Fe	0.038
Cd	0.0016
B	>0.03
Sn	0.0033
Mg	0.0075
Cr	0.002
Ni	0.0025
Mn	0.004
Ti	0.003
V	0.003
Bi	0.0023
Al	bal.

Table 2

ELEMENT	COMPOSITION, w/o
C	0.23
Mn	0.39
Si	0.04
Ni	0.01
Cr	0.03
Mo	<0.01
S	0.011
P	0.008
Cu	0.02

Table 3

SPECIMEN NUMBER	SLOPE PARAMETER, Ω-m^2	VELOCITY, m/s	STEADY-STATE POTENTIAL, v (Ag/AgCl)
I-32/03		0.03	-1.04
I-32/09	0.32	0.09	-0.98
I-32/30		0.30	** -0.88
I-63/03		0.03	-1.00
I-63/09	0.63	0.09	-0.90
I-63/30		0.30	** -0.84
I-194/03		0.03	-0.89
I-194/09	1.94	0.09	*1,** -0.78
I-194/30		0.30	*1 -0.67
I-385/03		0.03	-0.71
I-385/09	3.85	0.09	*1 -0.68
I-385/30		0.30	-0.66

*1: Exception 1, Type 1 (see Text for explanation).
**: Exception 2 (see Text for explanation).

Table 4

SPECIMEN NUMBER	SLOPE PARAMETER, Ω-m^2	VELOCITY, m/s	STEADY-STATE POTENTIAL, v (Ag/AgCl)
II-081/03		0.03	-1.05
II-081/09	0.081	0.09	-0.98
II-081/30		0.30	***
II-17/03		0.03	-1.04
II-17/09	0.17	0.09	-0.99
II-17/30		0.30	*1,***
II-32/03		0.03	-1.05
II-32/09	0.32	0.09	*2 -0.96
II-32/30		0.30	*1,***
II-63/03		0.03	-1.04
II-63/09	0.63	0.09	*1,*2 -0.97
II-63/30		0.30	*1 -0.78

Note: Where no potential is listed, specimen did not reach steady-state.
*1: Exception 1, Type 1 (see test for explanation).
*2: Exception 1, Type 2 (see test for explanation).
***: Exception 3 (see text for explanation).

Table 5

SLOPE PARAMETER, Ωm^2	TIME, hrs	CATHODE POT., ϕ_c, v.	ANODE POT., ϕ_a, v.	$\phi_c - \phi_a$, v.	ΔV ACROSS RESISTOR, v
0.081	3,740	-0.689	-0.700	0.011	0.011
	3,915	-0.709	-0.720	0.011	0.011
	4,035	-0.695	-0.707	0.012	0.012
	4,165	-0.695	-0.706	0.010	0.011
0.17	3,740	-0.669	-0.691	0.022	0.021
	3,915	-0.673	-0.693	0.020	0.020
	4,035	-0.671	-0.689	0.018	0.019
	4,165	-0.67	-0.687	0.017	0.016
0.32	3,740	-0.832	-0.952	0.120	0.119
	3,915	-0.796	-0.926	0.130	0.130
	4,035	-0.775	-0.900	0.125	0.125
	4,165	-0.777	-0.897	0.120	0.119

Table 6

SEA WATER VELOCITY, m/s	POTENTIAL, v (SCE)	DEPOSIT THICKNESS, mm
0.30	-1.03	0.18
	-0.93	0.07
	-0.78	0.04
0.08	-1.03	0.06
	-0.93	0.05
	-0.78	0.03

Table 7

POTENTIAL (approximate) v, (Ag/AgCl)	PORO SITY (unit less)	
	0.09 m/s	0.30 m/s
-0.78	0.035	0.061
-0.89	0.086	0.104

Figure 1: Schematic illustration of (a) a steel cathode specimen and (b) an aluminum anode specimen after machining.

Figure 2: Schematic side view representation of the test cell layout.

Figure 3:   **Schematic side view rendering of the first experiment setup.**

Fresh Sea
Water
⇩

Recirculation From Pump
⇐

Excess Sea Water Runoff
⇒

Sea Water
Drain

Upper Reservoir

Flow
Direction

Lower Reservoir

Test Lines

Velocity
Control
Valves →

Pump
Flow
Valve

Pump
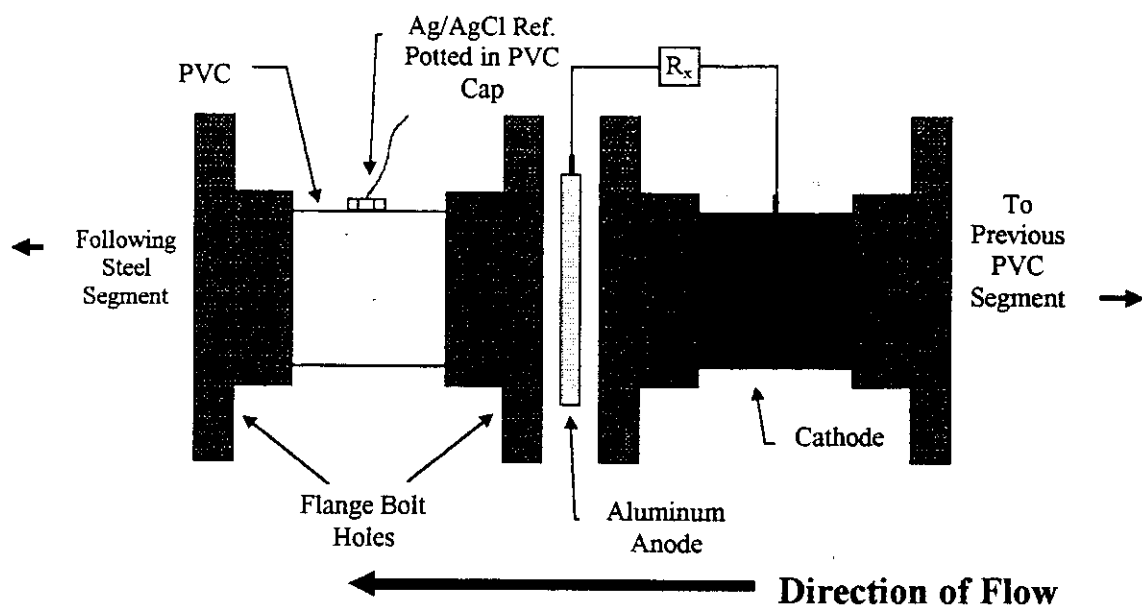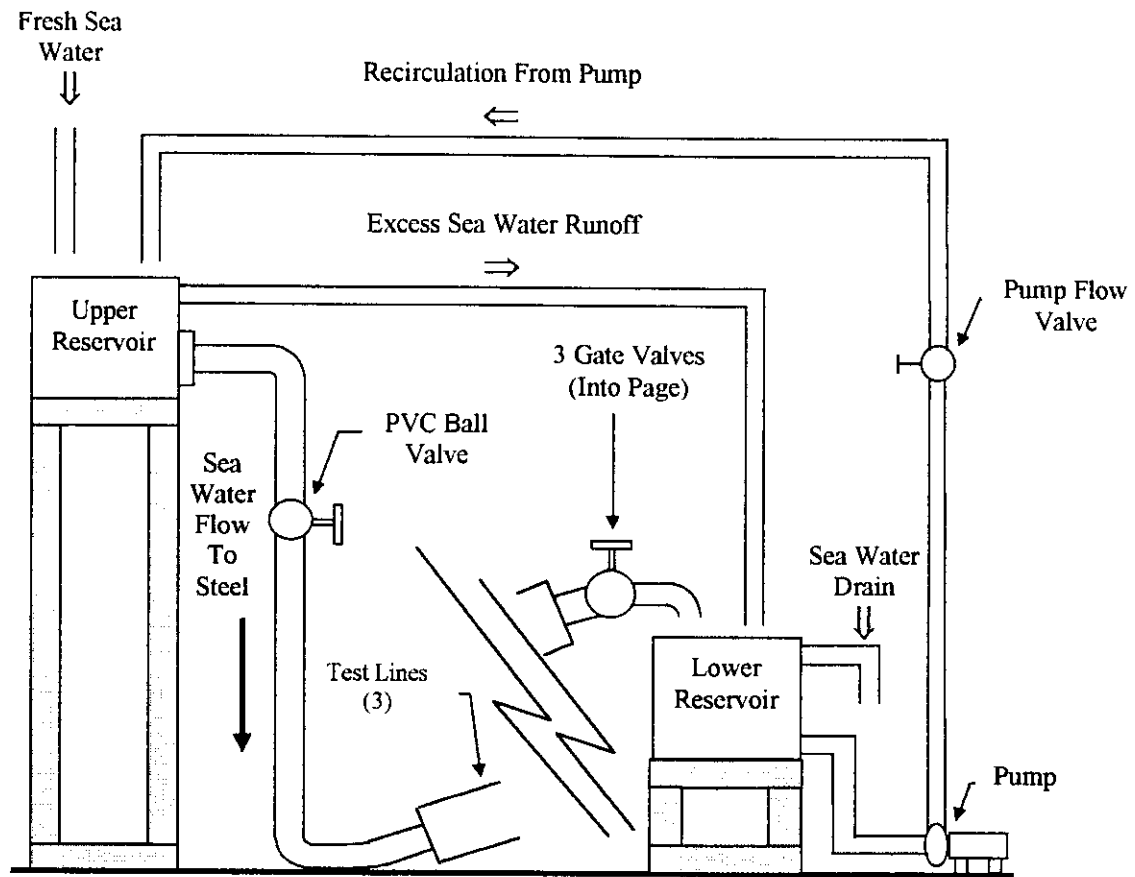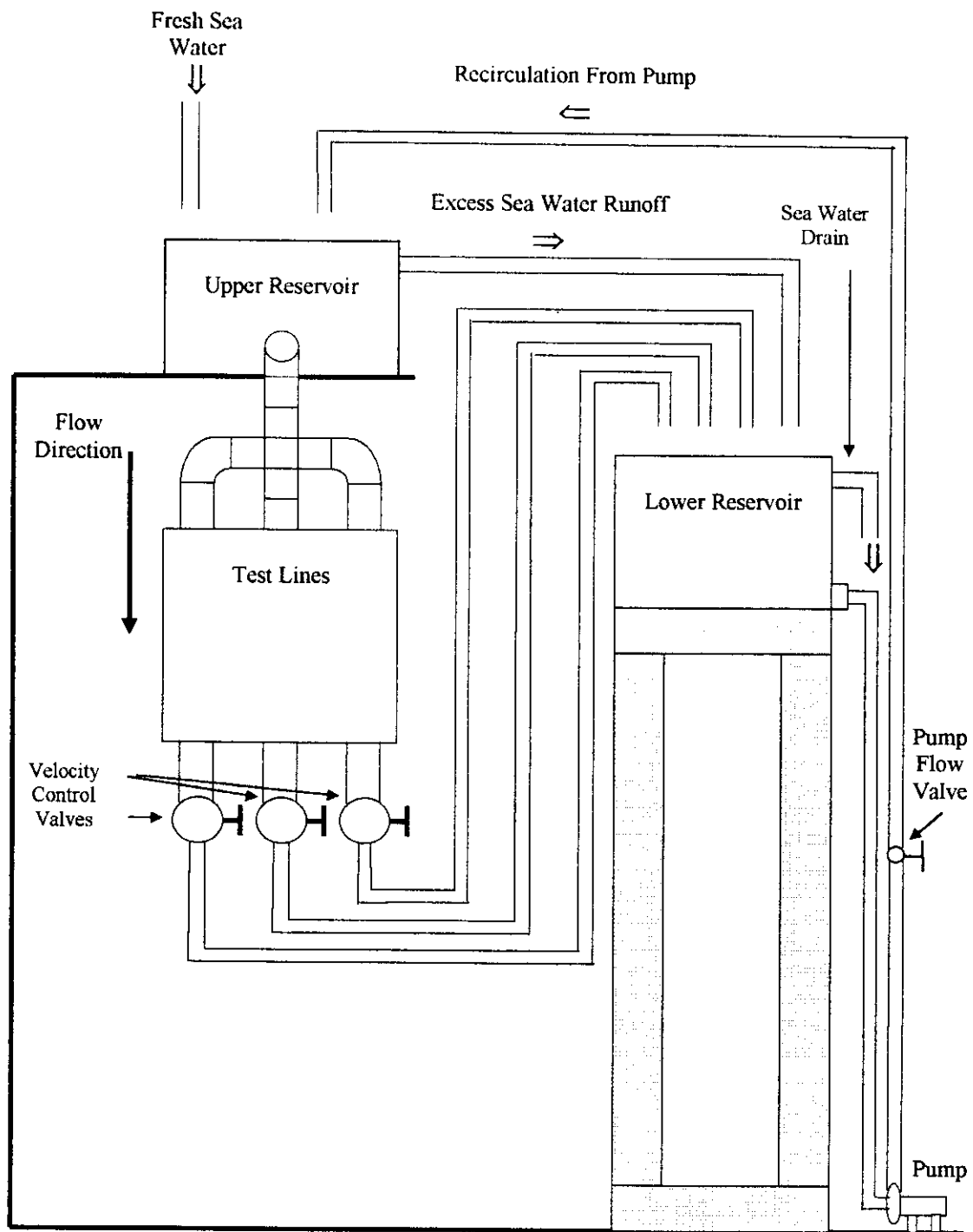
Figure 4:   Schematic front view illustration of the second experiment setup.
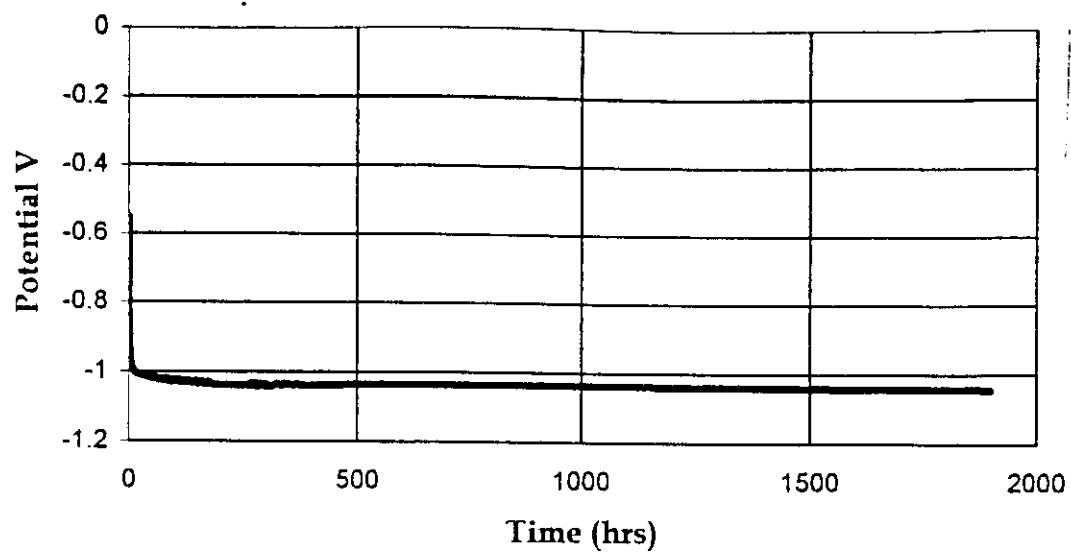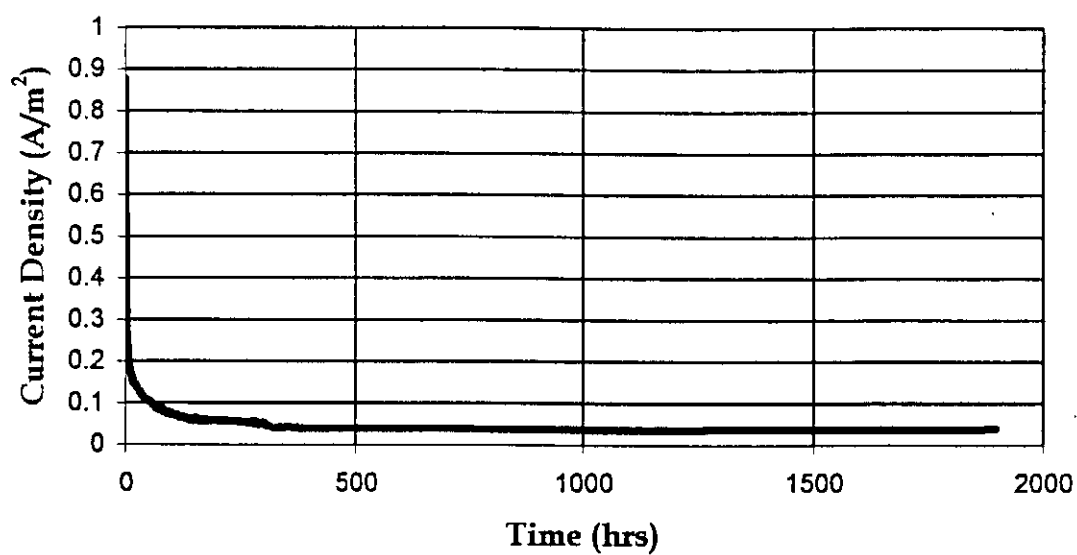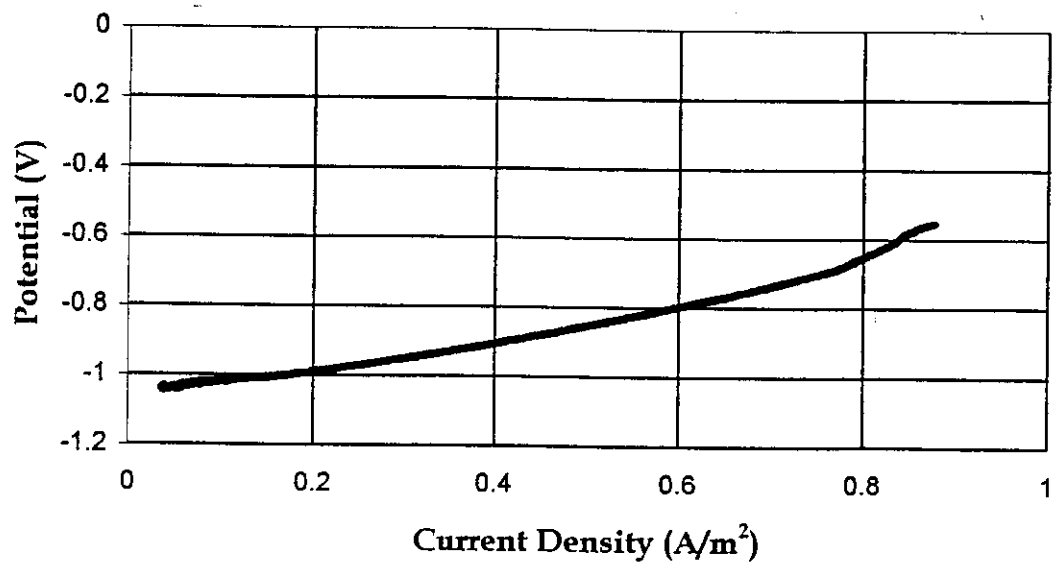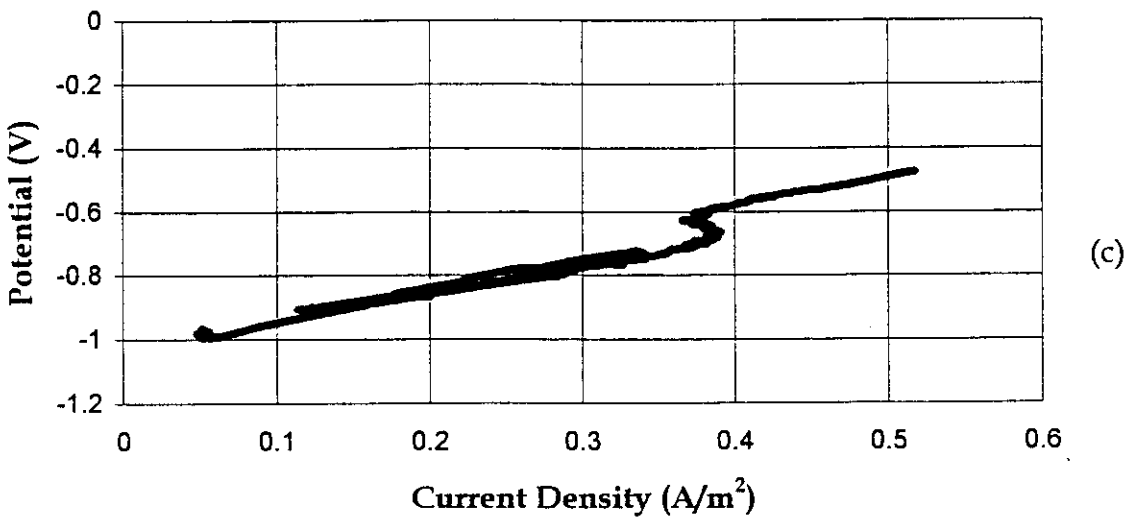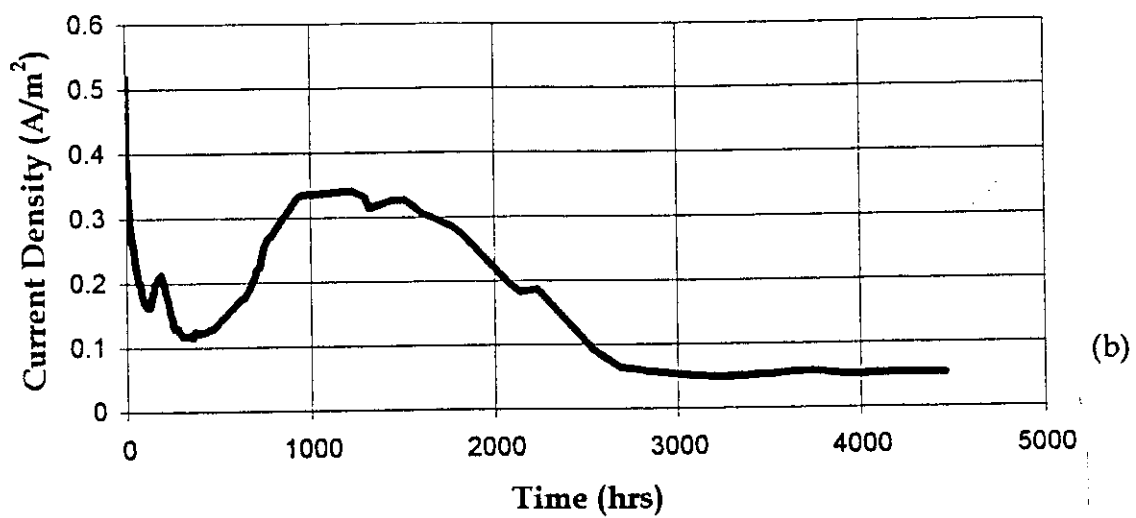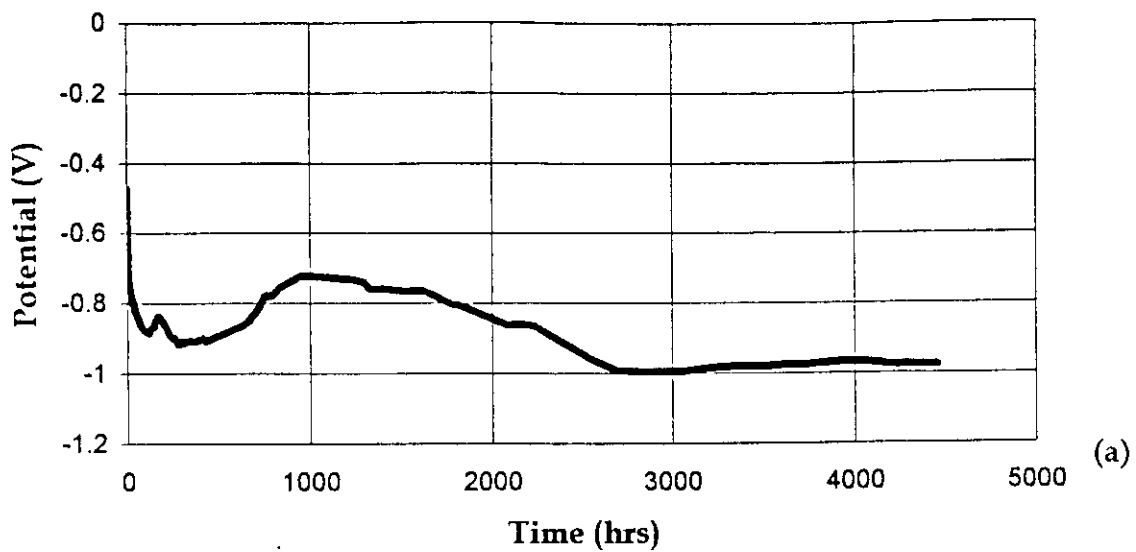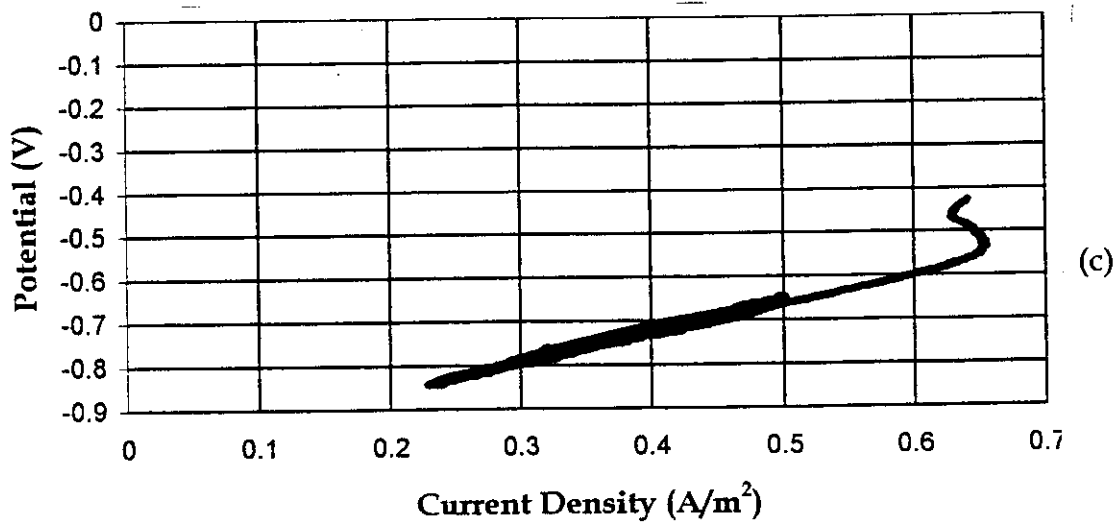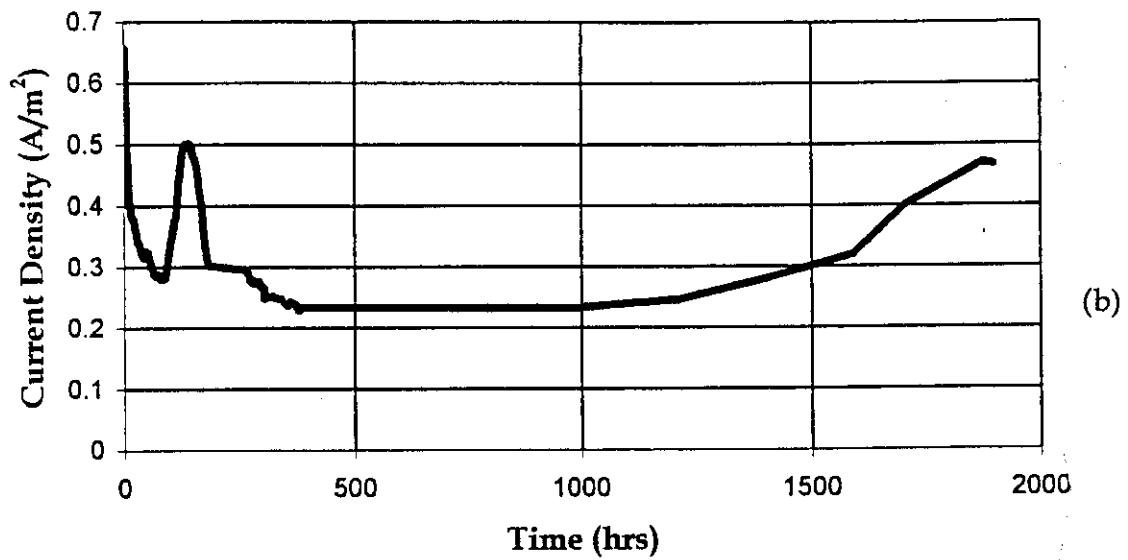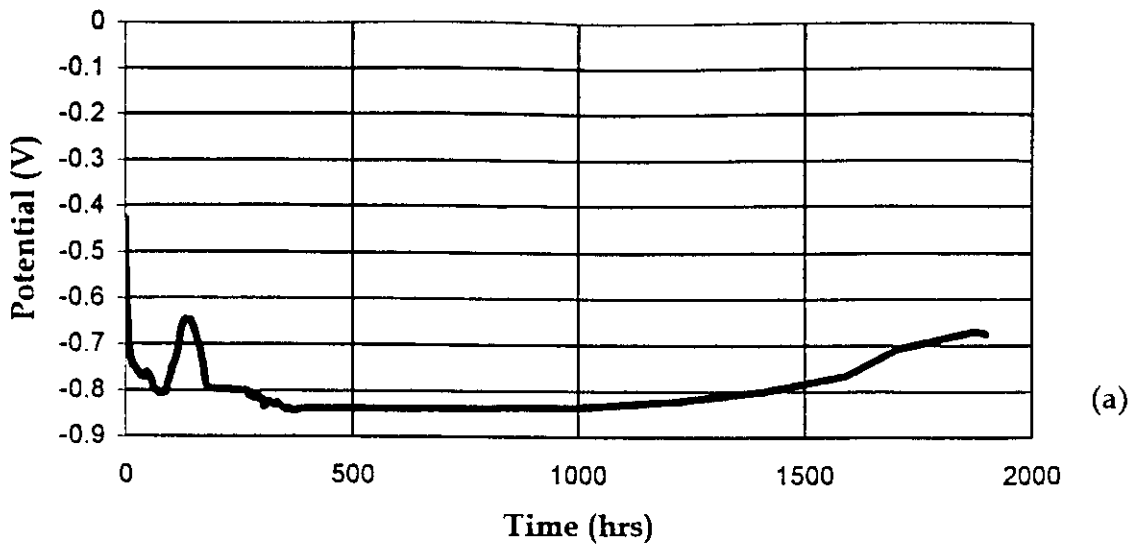
Figure 5:

Figure 6:

Figure 7:
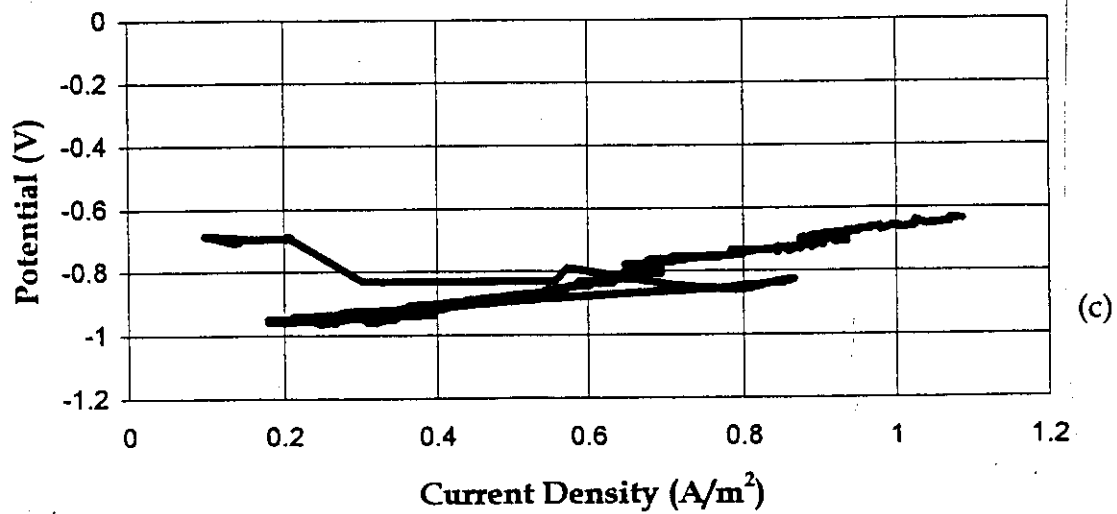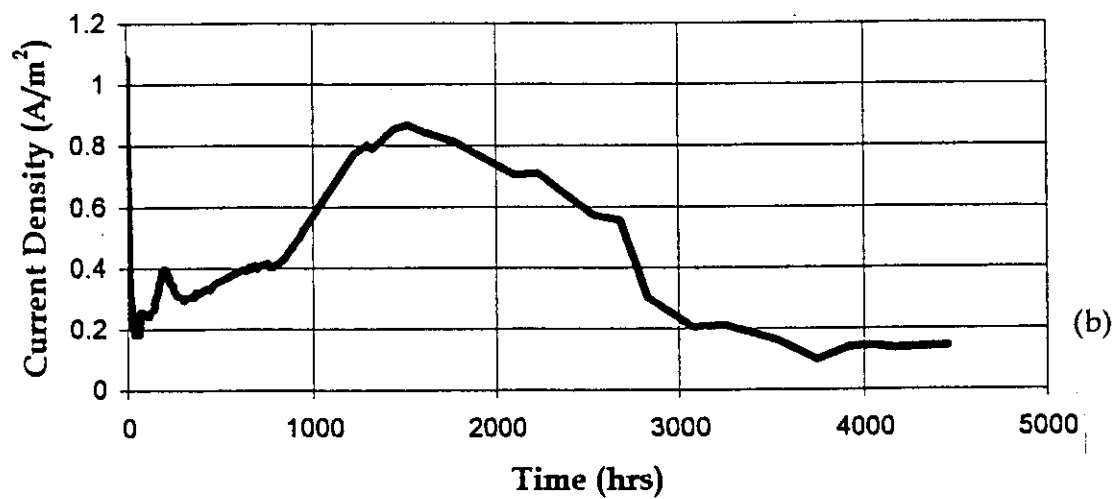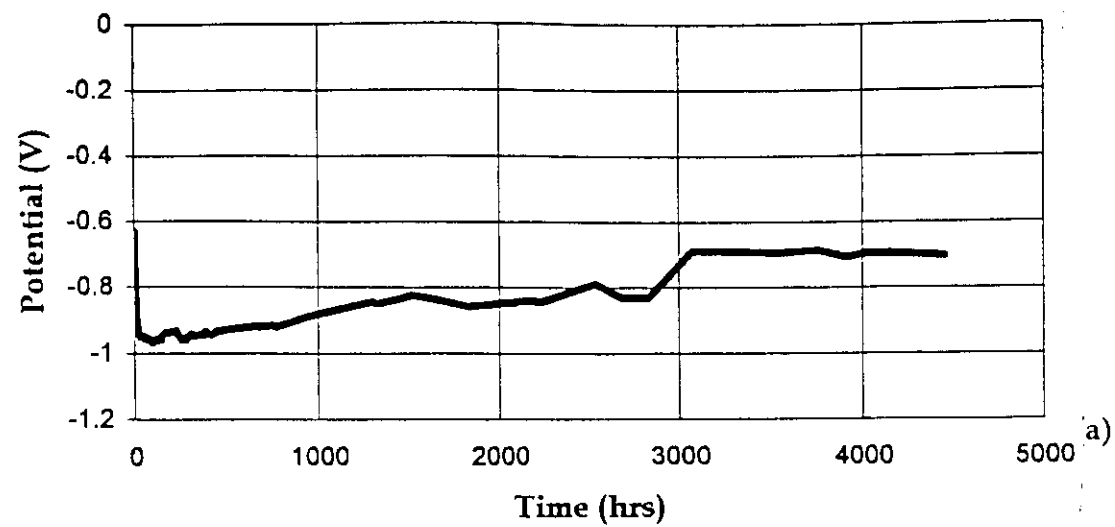
Figure 8:
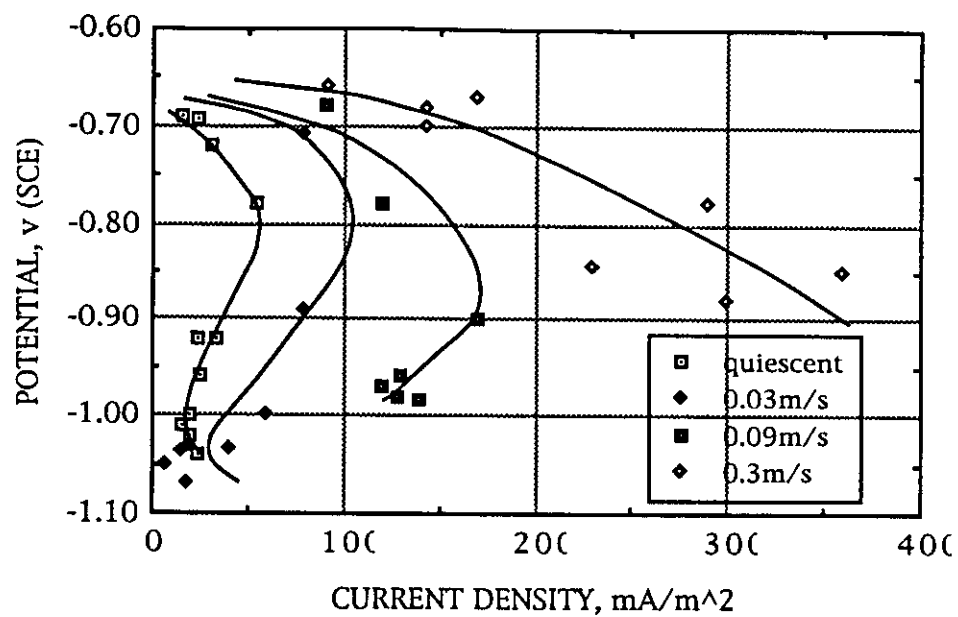
Figure 9
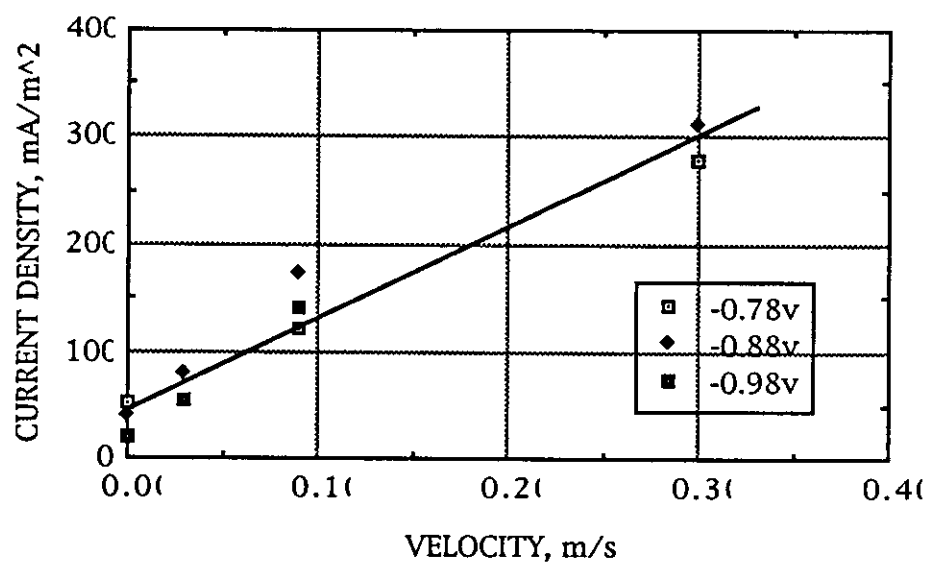
Figure 10
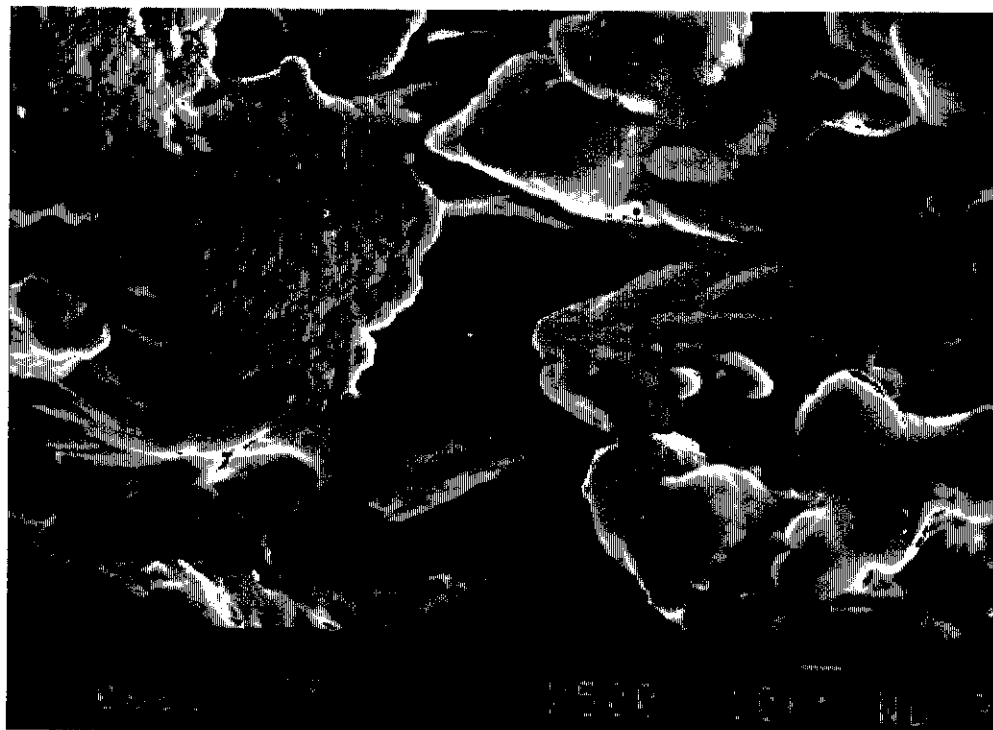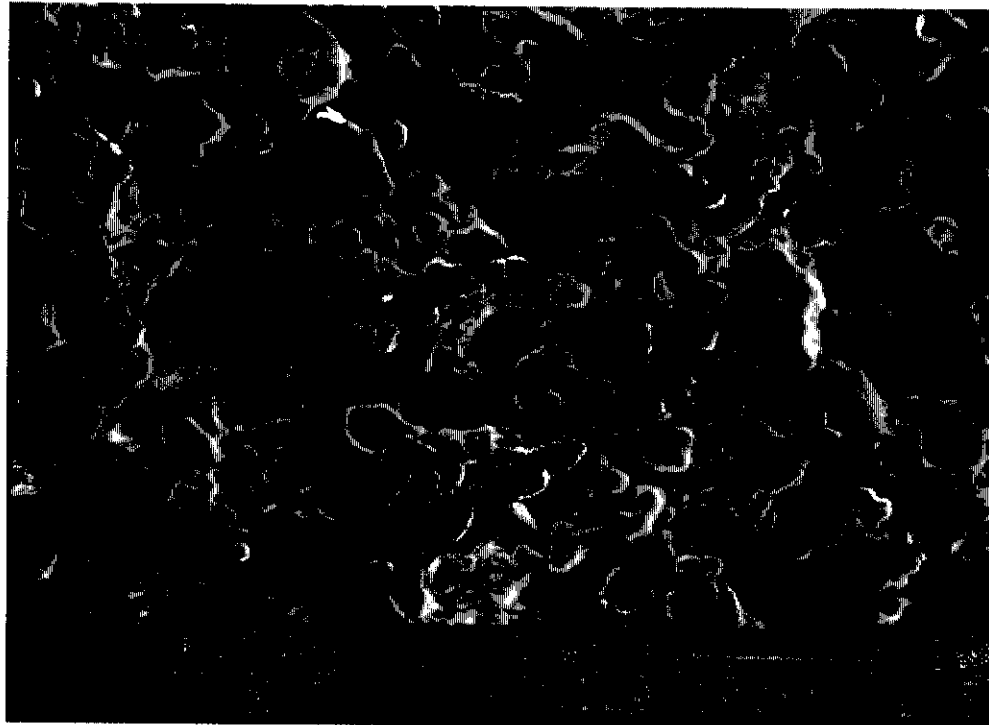
Figure 11:
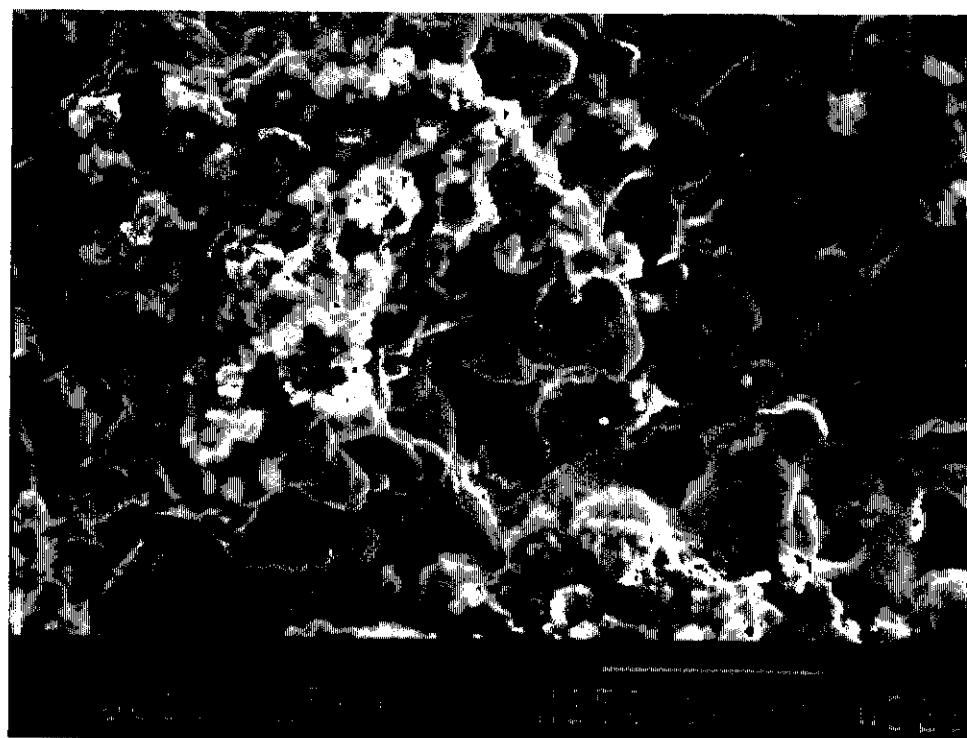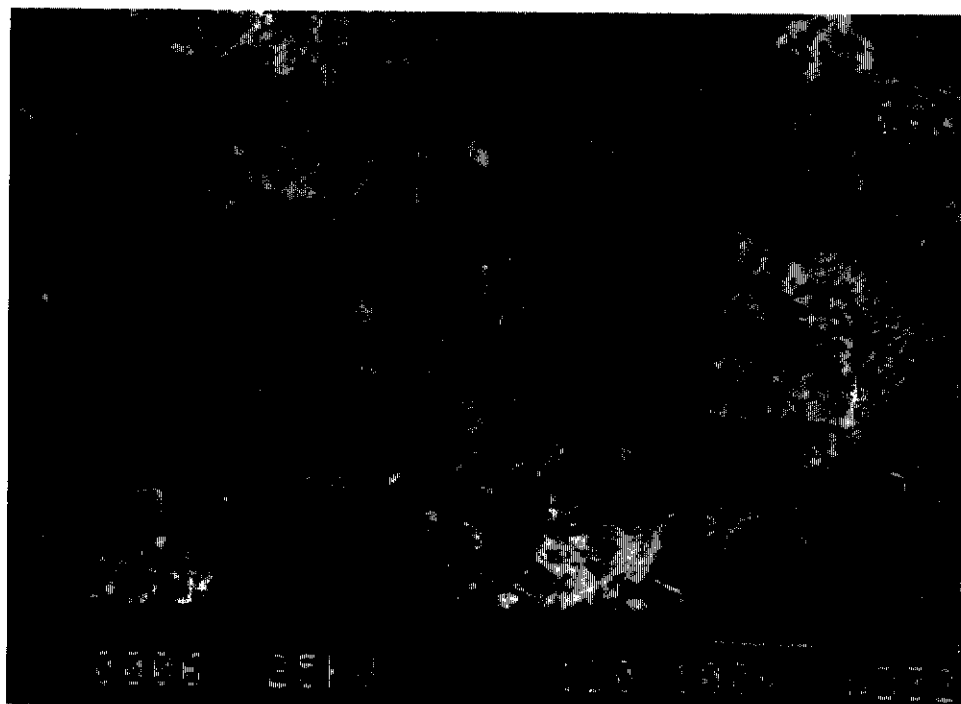
Figure 12:
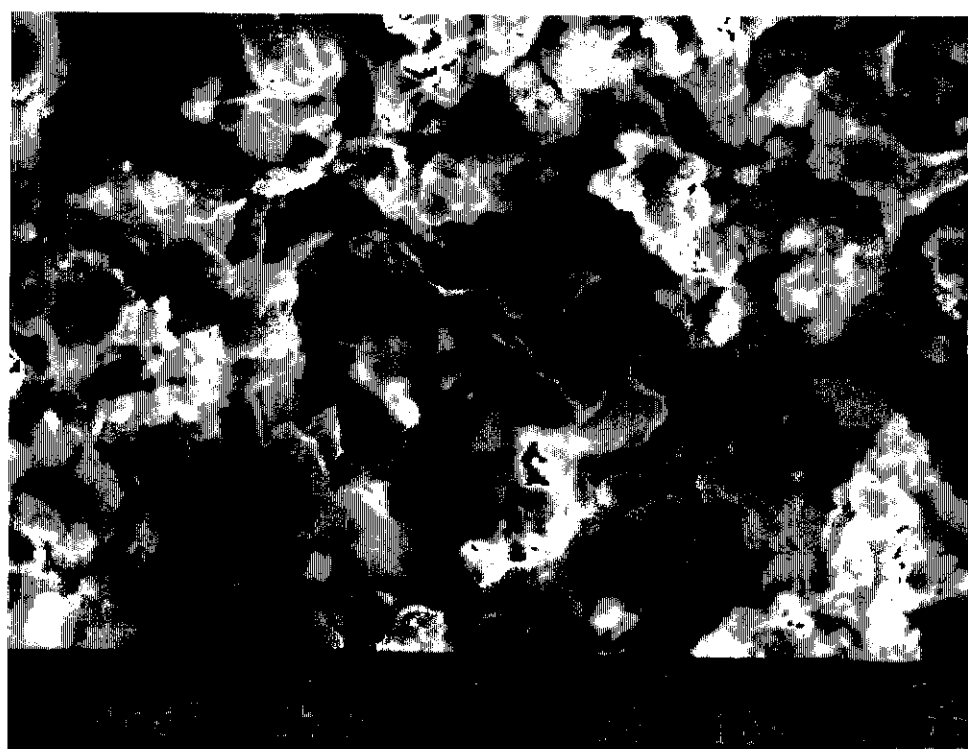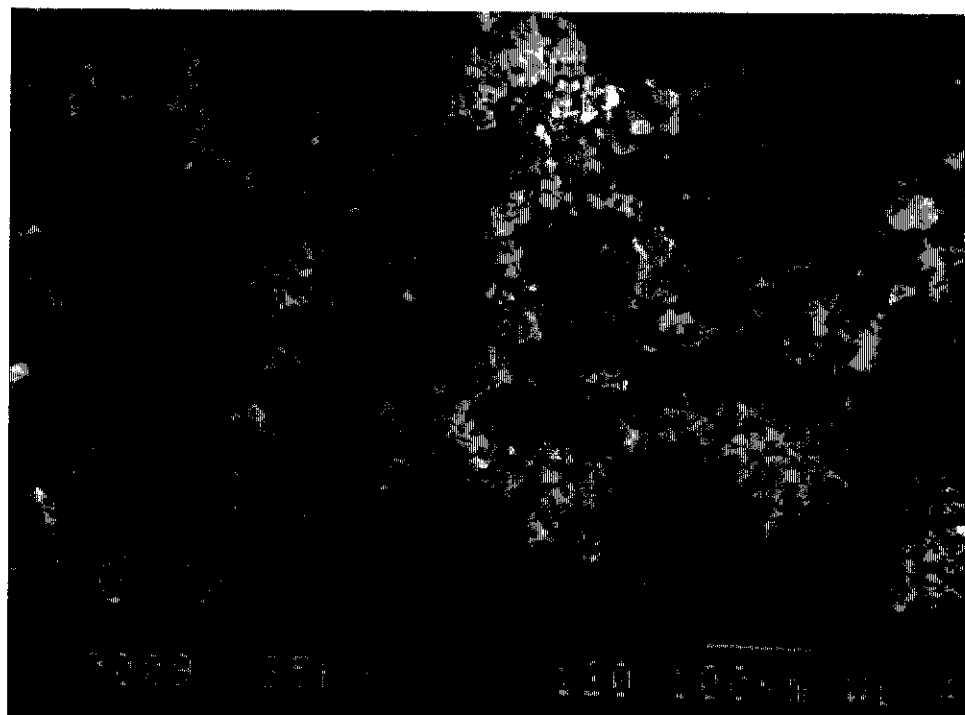
Figure 13:
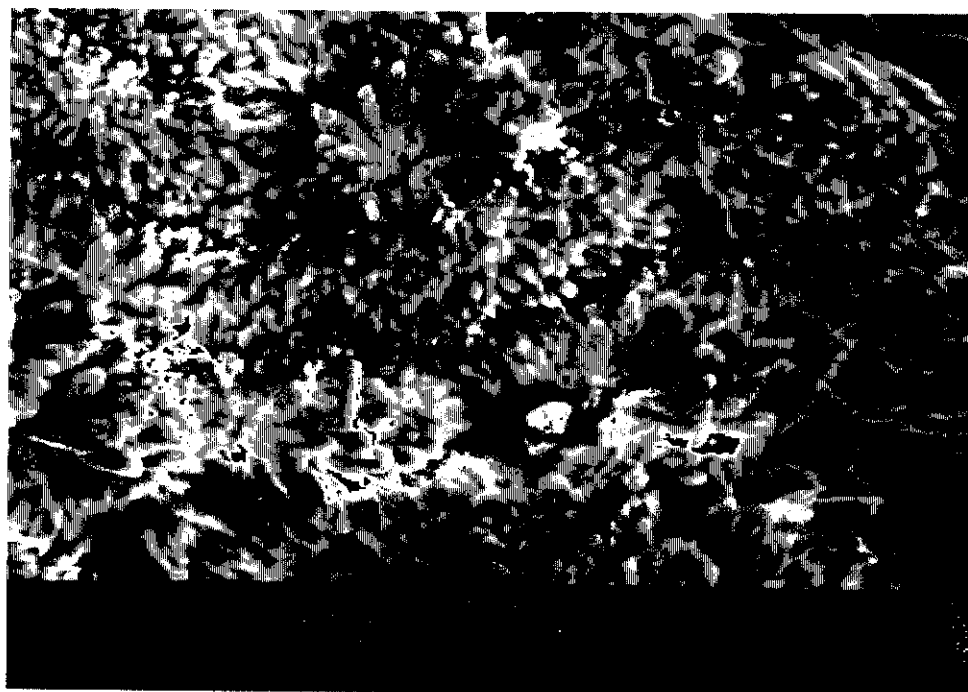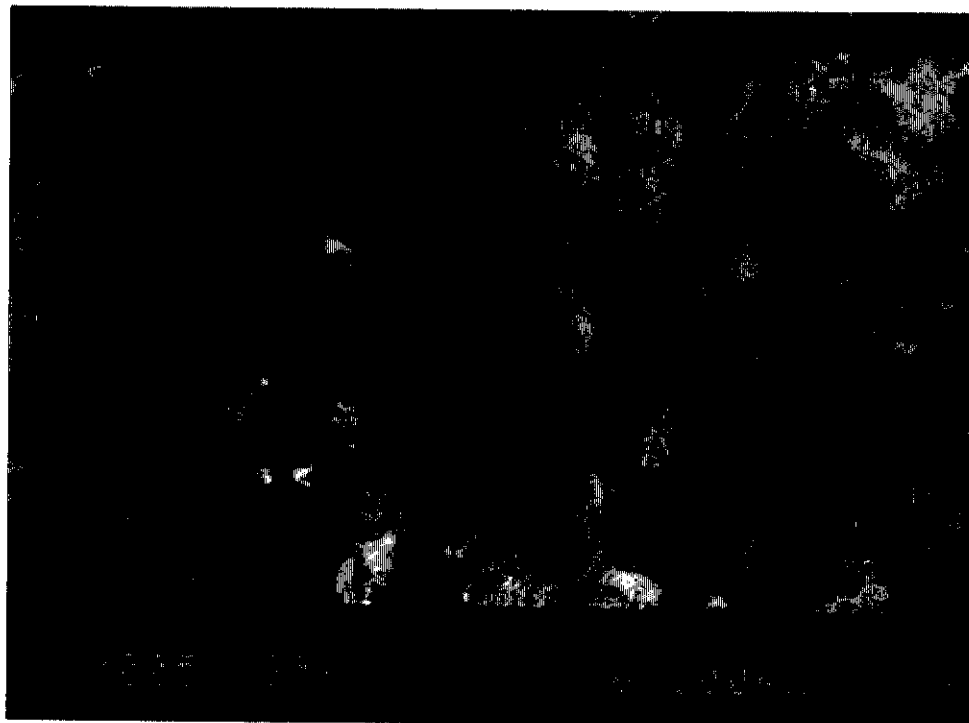
Figure 14:

Figure 15:

Figure 16: